Martin Gattringer

Numerical simulation of drop impact on dry and wetted surfaces

Diplomarbeit

zur Erlangung des akademischen Grades eines Diplomingenieurs

Studienrichtung: Maschinenbau

Technische Universität Graz
Erzherzog-Johann-Universität
Falkultät für Maschinenbau

Betreuer: Ao.Univ.-Prof. Dipl.-Ing. Dr. Helfried Steiner (TU Graz)
Dr. Vladimir Titarev (Cranfield University, UK)

Vorgelegt am: Institut für Strömungslehre und Wärmeübertragung

Technische Universität Graz

Graz, 2010

Deutsche Fassung:

Beschluss der Curricula-Kommission für Bachelor-, Master- und Diplomstudien vom 10.11.2008. Genehmigung des Senates am 1.12.2008

EIDESSTATTLICHE ERKLÄRUNG

Ich erkläre an Eides statt, dass ich die vorliegende Arbeit selbstständig verfasst, andere als die angegebenen Quellen/Hilfsmittel nicht benutzt, und die den benutzten Quellen wörtlich und inhaltlich entnommenen Stellen als solche kenntlich gemacht habe.

Graz, am Unterschrift

Englische Fassung:

STATUTORY DECLARATION

I declare that I have authored this thesis independently, that I have not used other than the declared sources/resources, and that I have explicitly marked all material which has been quoted either literally or by content from the used sources.

Graz, Signature

Acknowledgement

I would like to thank my project supervisor Dr. Vladimir Titarev. His availability at any time and imaginative ideas for improvement of the present work has been an important help. I also would like to thank my supervisor Prof. Helfried Steiner. I never missed support despite the huge distance between Cranfield and Graz.

I would also like to express my gratitude to Dr. Evgeniy Shapiro. His ability to answer questions has been enlightenment over the whole year in Cranfield. Moreover I want to give my thanks to the other staff in Cranfield for their support.

I would like to thank my friends from the course for the good time we had together. Klementina and Hairol, you have been a good companions through the world inside and outside of the lab.

I also want to acknowledge the people from Cranfield, especially the people from “The Drive”, for the family they gave me as I was far from home.

I also would like to thank my parents, brothers and friends for giving me support through busy times.

Finally, I want to give my particular thanks to Barbara for the understanding and energy she gave me.

Kurzfassung

Der Aufprall eines Flüssigkeitstropfens auf trockene und mit Flüssigkeit benetzte Oberflächen wurde mit dem kommerziellen Programm FLUENT 6.3.26 simuliert. Das Hauptaugenmerk dieser Arbeit liegt in der Prüfung der Vorhersagefähigkeit der CFD-Software mittels der implementierten „Volume of Fluid“ Methode in Bezug auf die physikalisch komplexen Bewegungen, die nach dem Kontakt und Aufprall eines Flüssigkeitstropfens auftreten.

Es wurden die Auswirkung verschiedener räumlicher Diskretisierungen untersucht, um ein angemessenes Rechengitter zu erhalten. Die Simulationen wurden mit einer breiten Variation des Tropfendurchmessers und der Aufprallgeschwindigkeit durchgeführt. Um verschiedene Benetzungsverhalten zu simulieren, wurde der Kontaktwinkel der Flüssigkeit-/trockene Oberflächepaarung variiert. Der Fokus der qualitativen und quantitativen Vergleiche liegt auf typischen Strömungsphänomenen wie der Formation und radialen Ausbreitung einer Flüssigkeitskrone beim Tropfenaufprall auf einer bereits mit Flüssigkeit benetzten Oberfläche, sowie auf der Ausbreitung der Flüssigkeit nach dem Tropfenaufprall auf trockener Oberfläche.

Die durchgeführten Simulationen zeigen ein realistisches Strömungsverhalten für den Aufprall eines Flüssigkeitstropfens auf benetzter Oberfläche. Spezielles Strömungsverhalten wie eine sich radial ausbreitende Flüssigkeitskrone und die Bildung von sogenannten Sekundärtropfen wurden in einer realistischer Art und Weise erhalten. Die qualitativen Simulationsergebnisse für den Aufprall auf trockener Oberfläche zeigen ebenso ein realistisches Verhalten, jedoch zeigen einzelne Phasen der Ausbreitung des Flüssigkeitsfilmes quantitativ hohe Abweichungen zu experimentellen Vergleichsdaten. Weiters wurden Empfehlungen für zukünftige Simulationen des Tropfenaufprallproblems vorgeschlagen.

Abstract

The impact of a liquid drop on wetted and dry surfaces is simulated using the commercial code FLUENT 6.3.26. The main objective is to investigate the capability of this commercial CFD software using the implemented Volume of Fluid method to capture the physically complex motion of the liquid after the moment of impact.

The effect of different grid resolutions was investigated to obtain an appropriate computational mesh. The simulations were carried out imposing a wide variation of the initial drop velocities and drop diameters. In order to simulate different wettabilities of the surface, the contact angle has been varied. The focus of the qualitative and quantitative evaluation of the computational results is put on different typical flow features like the formation and propagation of a radial crown for impacts on wetted surfaces covered by a pre-existing film, or the spreading of the liquid after an impingement on dry surfaces.

The present simulations feature a realistic flow behaviour for the impact on wetted surfaces. Particular flow phenomena like a radially extending crown and the formation of secondary droplets are obtained in a realistic manner. The qualitative assessment for an impacting drop onto dry surfaces shows a realistic behaviour as well. The individual stages of the spreading process after the impact show quantitatively high differences to experimental data though. Recommendations are made for future simulations of the drop impact problem.

Keywords: Drop impact; Volume of Fluid method; Splashing; Spreading; Pre-existing Liquid Film; Dry Surface.

Contents

List of figures

List of tables

Nomenclature

c_p	Specific heat capacity
d^*	Spread factor, $d^*=r/R$
D	Initial drop diameter
E_S	Surface energy
f_i	Body forces
g	Gravitational acceleration
H	Dimensionless thickness of the liquid film
h_0	Thickness of the pre-existing liquid film
K	Dimensionless quantity (splashing limit)
Oh	Ohnesorge number
p	Pressure
Pe	Peclet number
R	Initial drop radius
Re	Reynolds number
t	Time
T	Dimensionless time, $T=t\cdot V_0/D$
T_{WY}	Dimensionless time, $T_{WY}=t\cdot\sqrt{(g/R)}$
u, v, w	Velocities in x, y and z direction
U	Dimensionless velocity, $U=u/V_0$
U_{WY}	Dimensionless velocity, $U_{WY}=u/\sqrt{(g\cdot R)}$
V	Volume
V_0	Initial drop velocity
We	Weber number
α	Volume Fraction in a single cell of the discretised domain
Γ_ϕ	Diffusion coefficient
η	Dynamic viscosity
Θ	Contact angle between wall and liquid drop
ρ	Liquid density
σ	Surface tension
τ	Shear stress
ϕ	Scalar property

Chapter 1 – Introduction

1.1 Motivation

The impact of fluid drops and drop chains on solid and liquid surfaces has a wide variety of applications, e.g. in the combustion chamber of engines, meteorology, jet printing or medical applications. The problem has been investigated in various experimental and theoretical studies. The latter analyzed in particular the formation of capillary waves and splashing phenomena in certain asymptotic limits. Assuming quasi-one-dimensional equations of motion, they mostly associate these equations with the thin liquid film flow approximation. In this work the impact of drops on thin liquid films as well as on dry surfaces has been examined numerically. The detailed physical mechanism of such an impact is not fully explored and the simulation is still a challenge for Computational Fluid Dynamics (CFD). The commercial solver FLUENT v.6.3.26 has been used as simulation tool. The VoF method is applied to track the dynamics of gas-liquid interfaces, as it is implemented in FLUENT for two-phase flow computations.

1.2 – Objectives

The aim of this work is to investigate the ability of the commercial solver FLUENT using the implemented Volume of Fluid method to capture the main two-phase flow phenomena occurring after the impact of a drop on a surface. The flow behaviour after the impact of a single drop onto dry and wetted surfaces shall be simulated.

Several investigations will be done in order to obtain an appropriate grid to resolve the characteristic flow features at feasible computational costs.

The simulated flow behaviour will be compared against previous numerical and experimental data as well as analytical solutions. The focus will be on characteristic flow phenomena following the impact. These will be for example the formation and the motion of the liquid crown for the impact on wetted surfaces or the spreading of the drop after its impingement on dry surfaces.

1.3 – Literature review

This literature review is targeted at addressing and explaining the following main topics relevant for the present work:

- The physics behind the impact of a liquid drop on a dry or wet surface, formation of a moving crown and secondary droplets at the crown rim
- Review of experimental studies carried out to investigate the presently considered flow configuration
- Review of the numerical studies of the considered two-phase flow and a brief description of the various methods which have been applied to capture the gas-liquid interface

1.3.1 Flow physics of a liquid drop impact

Multiphase flows are heavily influenced by the mechanical and thermodynamic behaviour of the interface between any two adjacent phases. The states of interacting materials can be characterized as solid, liquid and gaseous. One of the most relevant forces is the surface tension force. It is caused by the attraction between the liquid's molecules due to intermolecular forces and defined as force acting per unit length given by σ. It acts parallel as well as orthogonal to the surface. The action of the surface tension causes a pressure difference Δp between the liquid enclosed and the surrounding phase for the case of a droplet. The energy of the surface of a spherical droplet is given by

$$E_s = \int_V \Delta p \cdot dV = \int_0^R \frac{2\sigma}{R} 4\pi R^2 dR = 4\pi\sigma R^2 \tag{1.1}$$

with R being the radius and V the Volume of the drop.

The interfacial tension between two liquids is zero, if they are fully miscible. The influence of temperature differences on the surface tension is not important in the considered cases of this work and therefore ignored.

The flow phenomena associated with impinging droplets on solid or liquid surfaces are influenced by many different parameters, e.g., surface tension, drop diameter, drop velocity, liquid viscosity, density, surface roughness, and many more. These relevant

parameters are generally grouped into non-dimensional quantities, such as the Weber number and the Reynolds number.

Different regimes of liquid motion can be observed during the impact of liquid drops on dry and wet surfaces. The resulting motion of the liquid depends heavily on the initial conditions, such as impact velocity, drop diameter, ambient pressure or impact frequency in case of a drop chain. Let ρ be the liquid density, η the liquid dynamic viscosity, D the drop diameter, V_0 the impact velocity and h_0 the thickness of the pre-existing liquid film. The flow conditions are the essentially characterised by the following non-dimensional numbers:

$$We = \frac{\rho D V_0^2}{\sigma},\ Re = \frac{\rho D V_0}{\eta},\ Oh = \frac{\eta}{(\rho \sigma D)^{1/2}} = \frac{We^{1/2}}{\mathrm{Re}}, \tag{1.2}$$

$$K = We \cdot Oh^{-2/5}, \quad H = \frac{h_0}{D}, \quad Ca = \frac{\eta V_0}{\sigma}, \tag{1.3}$$

where *We*, *Re*, *Oh* and *Ca* denote the Weber, Reynolds, Ohnesorge, and Capillary numbers, respectively. *K* is an important composite group, and *H* defines the dimensionless fluid film thickness.

The impinging drop on a dry surface can behave in different ways after the impact. Depending on the boundary conditions, bouncing, spreading or splashing is possible as shown in Figure 1.1. If the drop is of ideal spherical shape, the first contact between the drop and the wall will be point like. Depending on the impact velocity, the pressure inside the drop can even reach the waterhammer pressure ($\rho \cdot c \cdot V_0$), where c is the speed of sound in the liquid. Indeed, even cavitation is possible.

In their experiments Rioboo *et al.* (2002) observed different stages in the recorded spreading curves. They divided the whole process into three stages. The beginning is characterised by the increase of the dimensionless contact diameter and called kinematic phase. The physics of the following spreading phase is more complicated because of the increasing influence of other parameters, e.g. surface roughness, or wettability. During this spreading phase, the droplet generally flattens to a pancake shaped lamella. The third phase defined by Rioboo *et al.* (2002) is the relaxation phase where the lamella starts to recede. They stated that the final outcome of the process can be quite different,

depending strongly on the magnitude of the receding contact angle. The spreading of a droplet is exemplarily shown in Figure 1.2, displaying a sequence of images obtained in simulations by Schroll (2009).

The contact angle is defined as the angle between the solid ground and the tangent of the liquid-gas interface at the contact point (Figure 1.3). The counting of the contact angle begins from the drop wetted ground inside the liquid. Advancing and receding contact angles are usually different but the difference can be negligible for hydrophobic surfaces as stated by Baldacchini *et al.* (2006). Surface roughness, surface structure and material are the main influences for the contact angle. Figure 1.3-c exemplarily shows a surface structure leading to a superhydrophobic behaviour.

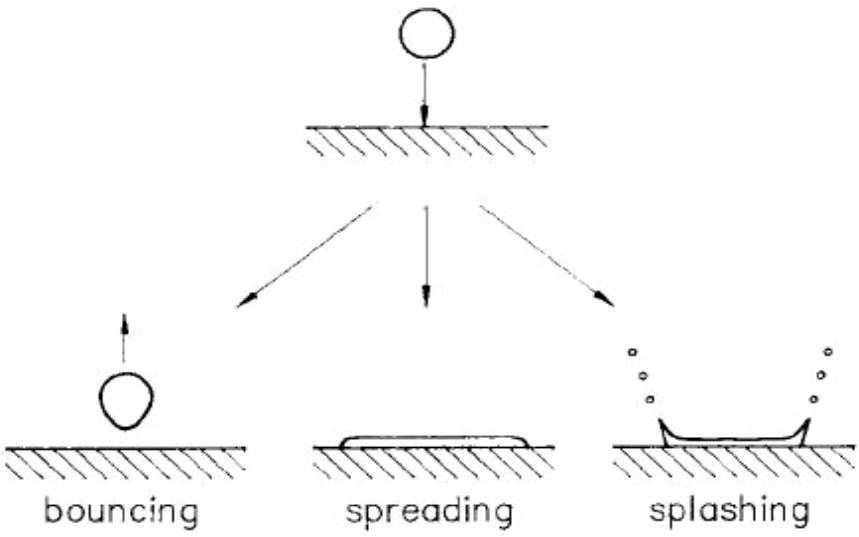

Figure 1.1: Impinging drop behaviour, from Rein (1993)

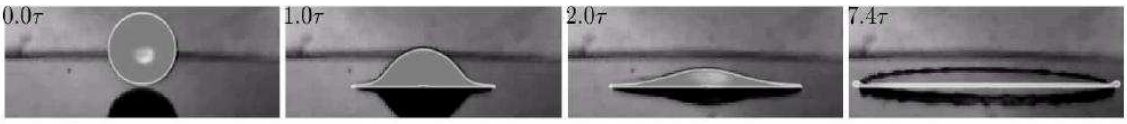

Figure 1.2: Spreading of a drop, from Schroll (2009)

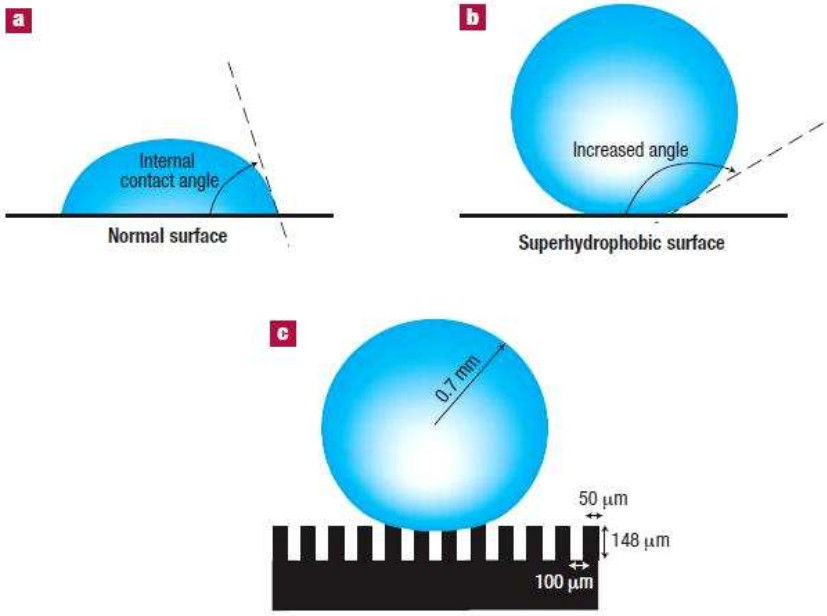

Figure 1.3: Liquid drop on different surfaces, from Quéré (2002)

The spreading of a drop on a solid surface is promoted by adhesive forces, while cohesive forces within the liquid work against it. A contact angle $\Theta=0°$ is associated with perfect wetting, while $\Theta=180°$ is associated with perfect non-wettability. For the demarcation between wetting and non-wetting the contact angle of 90° is commonly used. Hence, an angle $\Theta>90°$ defines a non-wetting liquid/solid combination.

In the case of a drop chain impinging on a dry surface only the first drop hits an absolutely dry surface. As a consequence, the wall shear stress conditions are different in the successive impacts. After the impact of the first drop, the wall has to be considered as wetted due the residual liquid on the surface. This changes the behaviour of the further impact process. The freight of the liquid film generated by the precursor droplets also depends strongly on the surface properties.

Rein (1993) stated that the compressibility of the liquid plays a major role during the initial phase of impact, while surface tension forces and the viscosity of the fluid are not important. Therefore, his main focus at the early stage of impact is merely on the initial fast deformation of the drop and the compression of the liquid. In contrast, the later behaviour depends strongly on the ambient pressure, on the kinetic energy of the impinging drop, and on the roughness of the surface.

Yarin (2006) considered the molecular wettability-induced slip as dominant near the contact line. But still this slip has a negligible effect on the spreading velocity. Therefore, the spreading motion is mainly driven by inertia and the gravitational force. The counteracting wall shear force in the boundary layer is proportional to the roughness of the surface. Mundo *et al.* (1995) consider the influence of this wall resistance to be negligible in case of a smooth surface. For low Reynolds numbers they further observed that there is not enough momentum normal to the surface to form a corona. The conclusion was that the kinetic energy, which is necessary to overcome surface tension and gravity, is dissipated due the initial deformation process. Clanet *et al.* (2004) stated that some part of the initial kinetic energy can also be transformed into an "internal" kinetic energy, associated with vertical motion emerging inside the deformed liquid.

Chandra and Avedisian (1991) observed the appearance/formation of a bubble at the point of impact in their experiments. They supposed two possible reasons for this. First, an entrapment of air during the impact process at the liquid-solid interface, and second, cavitation due to low local liquid pressure which they considered as the more unlikely mechanism though.

Despite the viscous effects during the spreading process, Davidson (1999) considered the spreading numerically as inviscid flow. He affirmed that the typical doughnut-like shape is the consequence of surface tension and inertia forces.

The rim around the liquid disk is of high interest, because the splash arises from this part of the interface. Hadfield and Stow (1981) concluded from their experiments, that the influence of the surface roughness is mainly responsible for generating instabilities in the emerging vertical water sheet. For the splashing itself the thickness of the watersheet is a crucial parameter. The findings of Hadfield and Stow (1981) proved the existence of a critical impact velocity for splashing in cases, where the length scale of roughness is small compared to the watersheet thickness.

Rein (1993) assumed the ambient gas to be of negligible influence, but Xu *et al.* (2005) showed that the presence of ambient gas can be of high importance for the occurrence of splashing. Both, the ambient gas pressure and the gas composition may influence the process. The surrounding gas provides the necessary counterforce due to the ambient

gas pressure to create the corona with a vertical component of momentum which leads to the appearance of a splash. Rioboo *et al.* (2001) identified the transition from deposition to splash for the impact on a dry surface as dependent of the dimensionless number *K*, defined in Equation 1.3. Below a certain value of *K*, which depends on the surface roughness, the impact ends in a spreading of the drop, while above this critical value of *K*, splashing occurs.

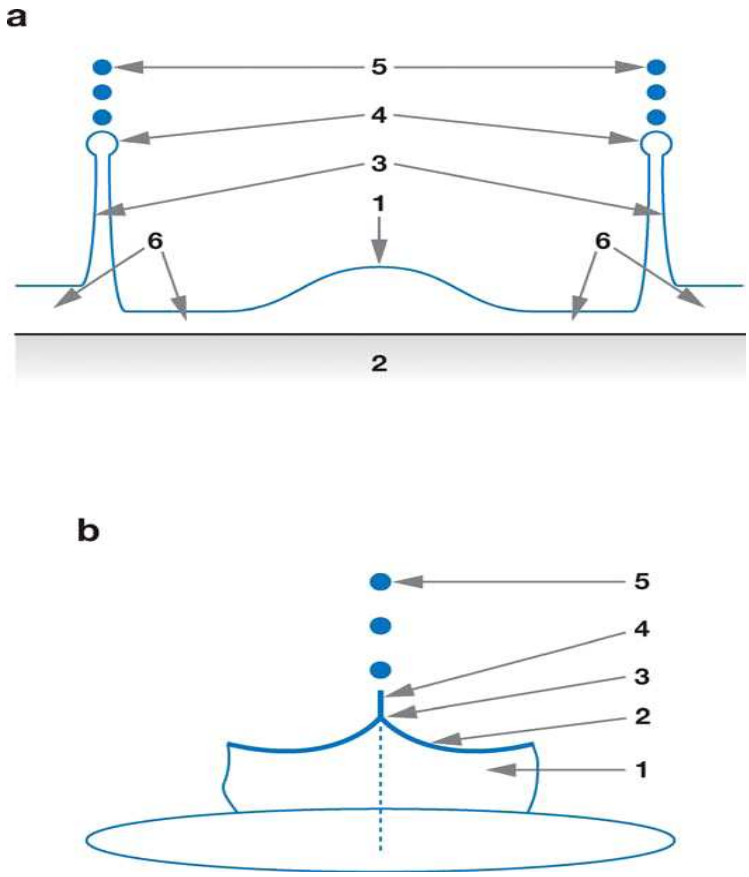

Figure 1.4: Sketch of splashing mechanism, (a) 1-residual top of impacting drop, 2-wall, 3-section of crown-like sheet propagating outward, 4-cross-section of free rim, 5-secondary droplets formed from cusps of free rim, 6-liquid layer on wall; (b) Free rim and secondary droplets magnified; 1-crown like sheet, 2- free rim at its top edge, 3-cusp, 4-thin jet emerging at cusp, 5-secondary droplets formed on breakup of jet, from Yarin and Weiss (1995)

Mundo *et al.* (1995) proposed a similar splashing criterion for both smooth and a rough dry surface given by Equation 1.4. For high/low values of K_d splashing or deposition without splashing occur.

$$K_d = Oh \cdot Re^{1.25} \tag{1.4}$$

During the splashing, mostly secondary droplets get ejected from the crown rim (Figure 1.4). These droplets separate from the wavy crown of the unstable rim during the last stages of splashing. Mundo *et al.* (1995) stated that the formation of these droplets depends on the fluid properties as well as on the kinematic parameters like impact velocity and size of the primary droplets in the case of a smooth solid surface.

In contrast to the impingement on a rough surface, no splash-corona occurs for a smooth surface, and the mean diameter of the secondary droplets decreases. After high speed impacts the fluid lamella often detaches from the solid surface before secondary droplets quarry out of the crown. Examining a drop impact on a thin liquid film Cossali *et al.* (2004) found an increase of the secondary droplet size as the splashing proceeds for higher impact velocities. They also state that in case of a pre-existing liquid film on the surface, the thickness of this liquid film plays no important role in determining the secondary droplet diameter.

Roisman and Tropea (2002) studied the drop impact on a surface with a pre-existing liquid film theoretically. They focussed on the following four regions of the drop and the liquid film: the perturbed liquid wall film inside the crown, the unperturbed film outside the crown, the rising jet forming a crown, and the free rim bounding the rising jet. Their theoretical model is valid for high-velocity impact of a low-viscosity drop on a relative thin liquid film. The model takes the inertial effects into account for the formation of the crown, but it neglects the surface tension as well as the viscous forces. The surface tension is not neglected for the motion of the free rim though. Their model showed quite good agreement with experiments and may therefore be considered as a realistic approach. However, the upper part of the crown is a highly unstable structure, bounded with a bumpy liquid rim. Roisman and Tropea (2002) describe the source of the crown as a distributed volume sink, which is introduced into the jump conditions written at the kinematic discontinuity at the base of the crown. Thus, balancing the mass loss at the discontinuity, a liquid film gets ejected from the kinematic discontinuity forming an upwards directed jet. As the height of the crown increases, small secondary droplets can be ejected from the upper rim (Figure 1.5).

Figure 1.5: Drop impact, from efluids.com

Levin and Hobbs (1971) mentioned that in the case of drop impact on a liquid surface the crown mainly originates from the target liquid. They observed only a slight difference between the splashing characteristics of impingement on a solid and a liquid surface. For the non-splash/splash transition Vander Wal *et al.* (2006) identified $Ca=0.35^{1/2}$ for impingement on a dry solid surface and $We=20^{1/2}$ for impingement on a thin liquid film as critical parameters, respectively. For values greater than the critical values splashing occurs.

Rioboo *et al.* (2003) observed for impacts on a liquid surface in the case of a deposition without formation of any crown or break up, that the flow features are similar to an impact on dry surface with complete wetting. They found for cases with high energy impacts that a decrease of the dimensionless fluid film thickness leads to a decrease of the temporal duration of the crown.

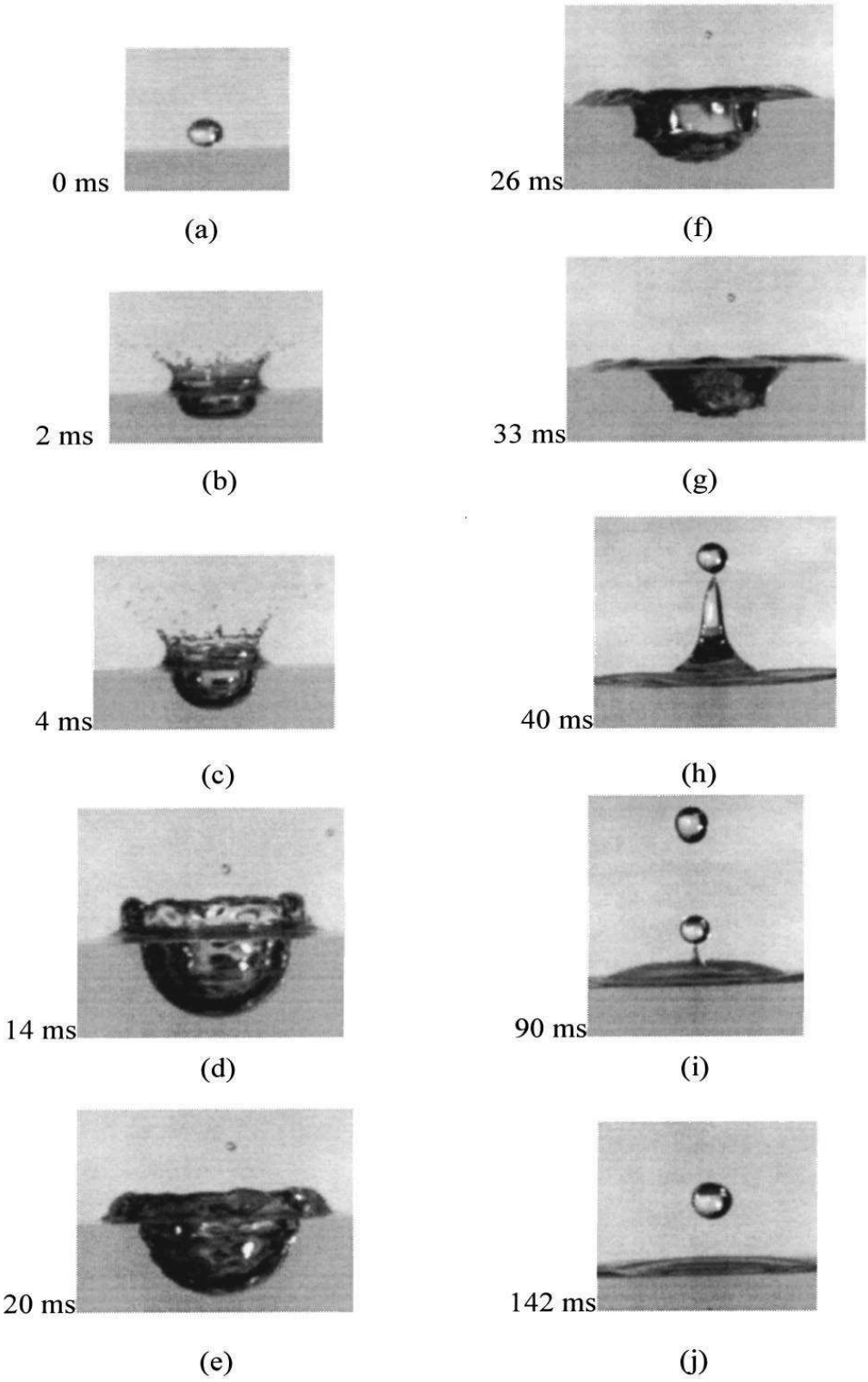

Figure 1.6: Sequence of a water drop impinging on a water pool, from Fedorchenko and Wang (2004)

Another possible flow feature of a drop impact on a liquid surface is the formation of capillary waves. Capillary waves may occur after drop impacts on liquid pools during the initial stages of the crater growth associated with the displacement of the target liquid by the drop liquid.

Morton *et al.* (2000) identified the swell of displaced target fluid collected at the mouth of the crater as the source of the capillary waves. The capillary waves thereafter propagate down the liquid wall of the expanding crater. The impact of a drop on a liquid pool can also produce a vertical Rayleigh jet after the crater has collapsed, as seen from Figure 1.6, t=40ms. The capillary instability further lead to the formation of secondary drops at the tip of the jet. Weiss and Yarin (1999) also observed the occurrence of capillary waves preceding the expanding crown which is generated in the splash after a drop impact onto a liquid film.

The full understanding of the contact phenomena between the drop and the surface of the target liquid is still an open research issue. Rein (2002) examined the capillary effect which can occur during the contact of two liquids. He showed that a possible uprise of pool liquid can be energetically favourable.

1.3.2 Previous numerical investigations

Several simulations with different multiphase models have been done in the past. The applied models generally rely on various assumptions and simplifications, e.g. Yarin and Weiss (1995). Taking the inertial, gravitational, viscous and surface tension terms into account, Xie *et al.* (2004) modelled the deformation process of a single droplet impingement onto a liquid film using a Moving Particle Semi-implicit (MPS) method. Fedorchenko and Wang (2004) suggested models for the maximum pool depth and central Rayleigh jet formation based on an energy consideration.

Applying a Lagrangian front-tracking numerical algorithm, Popinet and Zaleski (1999) obtained good results for damped oscillations of capillary waves.

Rieber and Frohn (1999) described the flow numerically by solving the incompressible Navier-Stokes equations in a two-fluid formulation and obtained physically reasonable

results. They considered variable density and viscosity and included the surface tension on the free interfaces.

A popular method for treating the interaction of particles is the Lattice Boltzmann Method (LBM). It is based on the mesoscopic kinetic theory. Therefore it can be considered as a phenomenological theory of macroscopic physical systems. E.g., Mukherjee and Abraham (2007) as well as Shi *et al.* (2008) used LBM to simulate drop impact hence the interactions.

A popular choice for numerical simulations of two-phase flows is the Volume of Fluid method (VoF). Nikolopoulos *et al.* (2005), Afkhami and Bussmann (2006), López *et al.* (2008), Schroll *et al.* (2009) are only a few examples of VoF-based numerical investigations which were carried out in the past for the impact problem.

The VoF-method is used in the present numerical simulations as well. A more detailed description of this method is given in section 2.1.2.1.

Chapter 2 – Mathematical formulation

2.1 – Governing equations

The task of Computational Fluid Dynamics is to describe the behaviour of a fluid flow numerically using mathematical models. The mathematical models should translate the physics into mathematical equations. These equations appear mainly in the form of partial differential equations. In essence, we formulate the conservation principles of mass, momentum and energy.

The numerical solution of these differential conservation equations is obtained in a discretised form.

2.1.1 Navier-Stokes equations

The Navier-Stokes equations are the governing equations of fluid dynamics and basis for the calculation of many flows. They are based on generic balance equations for mass and momentum of Newtonian fluids. In Newtonian fluids the dynamic viscosity represents a material property which is independent from the shear rate. Furthermore, the only occurring body force is mostly the gravitational force.

The physical meaning of the continuity equation is that mass can neither be created nor destroyed. Equation (2.1) gives the continuity equation written in stationary Cartesian coordinate system, hence, in an Eulerian frame of reference, where it reads

$$\frac{D\rho}{Dt}+\rho\left(\frac{\partial u}{\partial x}+\frac{\partial v}{\partial y}+\frac{\partial w}{\partial z}\right)=0\,. \tag{2.1}$$

$$\frac{D}{Dt}=\frac{\partial}{\partial t}+u\frac{\partial}{\partial x}+v\frac{\partial}{\partial y}+w\frac{\partial}{\partial z} \tag{2.2}$$

Therein, *u*, *v* and *w* are the velocities in the *x*, *y* and *z*-directions, respectively. The time dependence appears in the substantial derivative *D/Dt* as shown in Equation (2.2).

The momentum equations basically represent Newton's second law, which says that the total change of the momentum of a body with time is equal to the sum of the forces acting on this body. The occurring forces are the body forces, e.g. gravitational forces,

and the surface forces such as pressure and viscous forces. Indeed, in viscous fluids, viscous stresses (Equation (2.3)) only appear, as long as there is motion, while normal forces caused by pressure act in quiescent fluids as well. Newtonian fluids exhibit a linear correlation between the velocity gradients and the viscous stresses as shown in Equation (2.3). The momentum equations in Cartesian coordinates are given by Equations (2.4) to (2.6).

$$\tau_{ij} = \eta\left(\frac{du_i}{dx_j} + \frac{du_j}{dx_i}\right) \tag{2.3}$$

x – Momentum:

$$\rho\frac{Du}{Dt} = f_x - \frac{\partial p}{\partial x} + \left[\frac{\partial \tau_{xx}}{\partial x} + \frac{\partial \tau_{xy}}{\partial y} + \frac{\partial \tau_{xz}}{\partial z}\right] \tag{2.4}$$

y – Momentum:

$$\rho\frac{Dv}{Dt} = f_y - \frac{\partial p}{\partial y} + \left[\frac{\partial \tau_{xy}}{\partial x} + \frac{\partial \tau_{yy}}{\partial y} + \frac{\partial \tau_{zy}}{\partial z}\right] \tag{2.5}$$

z – Momentum:

$$\rho\frac{Dw}{Dt} = f_z - \frac{\partial p}{\partial z} + \left[\frac{\partial \tau_{xz}}{\partial x} + \frac{\partial \tau_{yz}}{\partial y} + \frac{\partial \tau_{zz}}{\partial z}\right] \tag{2.6}$$

Therein, η is the dynamic viscosity, f_i are the body forces, p is the pressure and τ_{ij} the viscous stress tensor. The individual elements of the viscous stress tensor τ_{ij} are defined as follows:

tangential stresses:

$$\tau_{xy} = \tau_{yx} = \eta\left[\frac{\partial v}{\partial x} + \frac{\partial u}{\partial y}\right],\ \tau_{yz} = \tau_{zy} = \eta\left[\frac{\partial w}{\partial y} + \frac{\partial v}{\partial z}\right],\ \tau_{zx} = \tau_{xz} = \eta\left[\frac{\partial u}{\partial z} + \frac{\partial w}{\partial x}\right] \tag{2.7}$$

normal stresses:

$$\tau_{xx} = \eta\left[2\frac{\partial u}{\partial x} - \frac{2}{3}div\vec{v}\right],\ \tau_{yy} = \eta\left[2\frac{\partial v}{\partial y} - \frac{2}{3}div\vec{v}\right],\ \tau_{zz} = \eta\left[2\frac{\partial w}{\partial z} - \frac{2}{3}div\vec{v}\right] \tag{2.8}$$

2.1.2 Multiphase flows

In the case of multiphase flows the fluid consists of more than one phases. In fact, we can basically distinguish between two different kinds of multiphase flows. Firstly, we classify a disperse flow as a flow of many small particles, drops or bubbles, in a carrier phase and secondly, we classify a dense flow, where the individual phases continuously occupy larger regions of the flow field separated by often very complex interfaces.

A wide range of models has been proposed and tested in multiphase flows of different kinds. For the present work FLUENT 6.3.26 has been used as simulation tool. The multiphase model applied here was the Volume of Fluid (VoF) approach. An introduction into the VoF model is given below.

2.1.2.1 Volume of Fluid method

Hirt and Nichols (1981) introduced the VoF method for use in problems with free fluid boundaries applying Eulerian coordinates. They considered free boundaries as surfaces across which one or more variables are discontinuous. They also mentioned three main difficulties in the numerical treatment of such free boundaries:

1) discrete representation
2) time evolution
3) approximation of the interfacial boundary conditions

Hirt and Nichols (1981) defined a phase marker function F to capture the instantaneous position of the liquid. Its value is zero in the gaseous region and unity in the liquid region, which basically makes it to a step function. The volumetric average of F represents the fractional volume of a cell occupied by liquid. Hence, if the average is between zero and unity, the cell is only partly occupied by the liquid. Therefore, we call it a fractional Volume of Fluid (VoF) method.

Moreover, the orientation of the interface in a computational cell is determined by the direction, into which F changes most rapidly. Hence, the derivative of F gives the local normal vector on the interface. Using the cell value of F and the normal vector, the location and the orientation of the interface is determined, which is further used for the approximation of interfacial boundary conditions.

As for the numerical solution of the motion of the interface, Hirt and Nichols (1981) applied a flux-based formulation which is aimed to preserve the discontinuous character of the function *F*.

FLUENT tracks the interface(s) by solving a continuity equation for the volume fraction of the defined phases. The mathematical formulation of these transport equations for the volume fractions are given below. As such, the implemented VoF-based multiphase model can handle the motion of two or more immiscible phases by tracking their volume fractions in each computational cell for the existing fluids throughout the domain. The model is applicable to time-dependent simulations which meets the present requirements. The volume averaged density and viscosity of the fluid are obtained as

$$\rho = \sum_q \rho_q \alpha_q \ , \tag{2.9}$$

$$\eta = \sum_q \eta_q \alpha_q \ , \tag{2.10}$$

where α_q denotes the volume fraction of phase *q*. α_q can vary within the following range:

- $\alpha_q = 0$: the cell is empty of the phase *q*
- $\alpha_q = 1$: the cell is completely filled by phase *q*
- $0 < \alpha_q < 1$: the cell contains an interface between the phase *q* and other phases

Transport equation for the volume fractions

The continuity equation for each individual phase *q* is written as

$$\frac{\partial}{\partial t}(\alpha_q \rho_q) + \nabla \cdot (\alpha_q \rho_q \vec{v}_q) = S_{\alpha_q} + \sum_{p=1}^{n} (\dot{m}_{pq} - \dot{m}_{qp}) \ , \tag{2.11}$$

where $\dot{m}_{pq}$ is the mass transfer from phase *p* to phase *q* and $\dot{m}_{pq}$ is the mass transfer from phase *q* to phase *p*. S_{α_q} is a source term for a possible user-defined mass source. The fluxes for the advective transport terms are computed using special interpolation

schemes to obtain the values at the cell faces. Implicit schemes as well as explicit schemes are available for the time discretization.

Momentum equation

The momentum equation is formulated as shared field approximation. Adopting this approximation the velocity field is shared among the phases, and only a single momentum equation is solved. The dependence of the momentum equation of the volume fraction is incorporated through the properties ρ and η given by Equation (2.9) and Equation (2.10), respectively. Assuming incompressible flow the momentum equation reads

$$\frac{\partial}{\partial t}(\rho\vec{v}) + \nabla\cdot(\rho\vec{v}\vec{v}) = -\nabla p + \nabla\cdot[\eta(\nabla\vec{v} + \nabla\vec{v}^{T})] + \rho\vec{g} + \vec{F}_{\sigma}. \qquad (2.12)$$

The computation of the surface tension force $\vec{F}_{\sigma}$ is described below.

Surface tension and wall adhesion

The surface tension occurs at the interface between two different phases. This force is responsible for example for the formation of drops. The source of this force is the attraction between the molecules in a fluid. Due to this property the pressure inside a drop or bubble is higher than the ambient pressure, as it is described by the Young-Laplace equation,

$$p_2 - p_1 = \sigma\left(\frac{1}{R_1} + \frac{1}{R_2}\right), \qquad (2.13)$$

where p_2 is the pressure inside the drop/bubble and p_1 is the ambient pressure outside. R_1 and R_2 are the radii of curvature measured in two orthogonal directions.

The effects of the surface tension relative to viscous and inertial forces are measured by the values of the Capillary number *Ca* and the Weber number *We*, respectively. It can be neglected, if *Ca*»1 or *We*»1.

In the present work a constant surface tension σ is assumed. The surface tension model implemented in FLUENT is a continuous surface force model proposed by Brackbill *et al.* (1992). This approach models the surface tension force, which basically acts only on

the interface, as a volumetric force term. For the present case of two phases, the volumetric surface force term reads

$$\vec{F}_\sigma = \sigma \frac{\rho\kappa \nabla\alpha_1}{\frac{1}{2}(\rho_1 + \rho_2)} . \quad (2.14)$$

The curvature κ of the interface is calculated from local gradients of the volume fraction of phase 1. The importance of the surface tension in the drop impact problem can be estimated based on the dimensionless quantity *K* defined in Equation (1.3). If *K*»1, the surface tension forces are negligibly small as compared to the inertial forces.

Examples of the possible shape of a liquid droplet placed on a solid surface were schematically shown in Figure 1.3. The spreading of a drop on a solid surface is caused by adhesive forces, while cohesive forces within a liquid work against it. For a contact angle Θ_W=0°, complete wetting occurs, while for Θ_W=180° the contact surface would be a single point. For the demarcation between wetting and non-wetting, a contact angle of 90° is commonly used. Hence, an angle Θ_W>90° defines a non-wetting liquid/solid combination.

The wall adhesions model in FLUENT uses an assumed contact angle between the fluid and the wall to compute the surface normal vector $\hat{n}$ in cells near the wall. The surface normal is obtained by Equation (2.15), where Θ_W is the contact angle at the wall. $\hat{n}_w$ and $\hat{t}_w$ are the unit vectors normal and tangential to the wall, respectively, as seen in Figure 2.1. The obtained normal vector $\hat{n}$, Equation (2.15), is used to compute the local curvature as input into the volumetric force term for the surface tension given by Equation (2.14).

$$\hat{n} = \hat{n}_w \cos(\Theta_W) + \hat{t}_w \sin(\Theta_W) \quad (2.15)$$

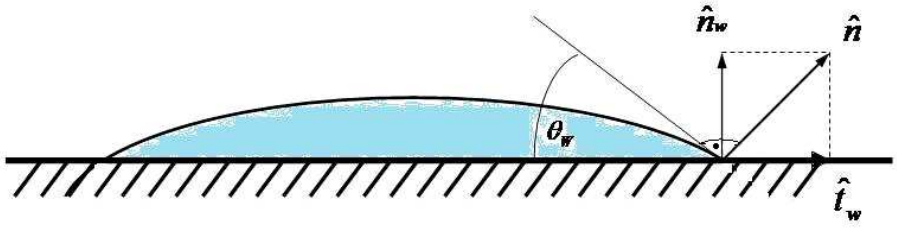

Figure 2.1: Sketch of the interface near the contact point

2.2 – Numerical solution

The numerical solution is obtained by solving the discretized governing equations. If no analytically exact solution is obtainable, the numerical methods provide a reliable tool to compute an approximate solution of the considered problem. The finally obtained solution is subject to various limitations and can therefore not be considered as an exact solution of the problem. The reasons for this deviation are summarized by Ferzinger and Peric (2002, p.24):

- *"The differential equations may contain approximations or idealizations;*
- *Approximations are made in the discretization process;*
- *In solving the discretized equations, iterative methods are used. Unless they are run for a very long time, the exact solution of the discretized equation is not produced. "*

The drop impact considered in the present work produces a flow field which varies spatially as well as temporally. An explicit VoF multiphase scheme has been used in the present simulations. A spatially first-order discretization scheme was used for the first time steps. Afterwards, a second-order scheme was applied to increase the accuracy of the solution in time.

The VoF method implemented in FLUENT allows only the use of a so called "pressure-based solvers". Thereby, the velocity field and the pressure field are computed by solving the momentum equation and a pressure, or pressure correction, equation. The pressure correction basically enforces the flow field to satisfy the continuity equation. The entire set of equations is solved iteratively until the solution is converged, or the desired accuracy is reached. Segregated as well as coupled algorithms are available.

The available advection schemes for the volume fraction equation are the Geometric Reconstruction scheme and High-Order Flux-limiting schemes.

2.2.1 Spatial discretization method - Finite Volume method

Various methods are available to discretize continuous equations, e.g. Finite Difference (FD), Finite Volume (FV) and Finite Element (FE) methods. FLUENT uses the Finite Volume method, which basically solves a volume integral of the governing conservation equations over the volume of each computational cell. These volume integrals are converted into algebraic equations which are suitable for numerical methods. The unsteady conservation equation of some arbitrary quantity ϕ can be generally written as

$$\frac{\partial \rho\phi}{\partial t} + \nabla \cdot (\rho\vec{v}\phi) = \nabla \cdot (\Gamma_\phi \nabla\phi) + S_\phi . \tag{2.16}$$

Integrating Equation (2.16) over a control volume *V* and invoking Gauss' divergence theorem yields

$$\int_V \frac{\partial \rho\phi}{\partial t} dV + \oint \rho\phi\vec{v} \cdot d\vec{A} = \oint \Gamma_\phi \nabla\phi \cdot d\vec{A} + \int_V S_\phi dV . \tag{2.17}$$

The approximation of (2.17) written as

$$\frac{\partial \rho\phi}{\partial t} V + \sum_f^{N_{faces}} \rho_f \vec{v}_f \phi_f \cdot \vec{A}_f = \sum_f^{N_{faces}} \Gamma_\phi \nabla\phi \cdot \vec{A}_f + S_\phi V \tag{2.18}$$

finally yields the volume average of ϕ for the considered control volume. The approximation for the integrals in (2.17) involve the surface area vector $\vec{A}$, a diffusion coefficient Γ_ϕ, a source of ϕ, S_ϕ, and the number of faces enclosing the cell N_{faces}. ϕ_f is the value of ϕ at the face *f*, $\rho_f \vec{v}_f \cdot \vec{A}_f$ the mass flux across the face and $\vec{A}_f$ the area of face *f*.

The considered flow domain is subdivided into a finite number of control volumes (CVs) by the grid. The conservation laws are applied to each of this CVs as well as to the whole domain. The discretization error decreases with refinement of the grid, hence it scales inversely with the number of CVs. The FV method basically computes the unknown scalar variables at the centre of the CV, i.e., at a "computational node". The fluxes are calculated at the faces of the CVs. Therefore, as the scalar values ϕ are

calculated at the cell centres, the corresponding face values ϕ_f have to be interpolated from the values at the cell centres.

2.2.1.1 Approximation of surface integrals and volume integrals

For 2D Cartesian control volumes, the surface consists of four (six in 3D) plane faces, denoted by their respective positions with respect to the centre, n, w, s, e, as shown in Figure 2.2. The net flux through the CV is the integral of the convective and/or diffusive fluxes across these faces. The face values are interpolated from the cell centre values. In order to avoid convergence and conservation problems, the control volumes should not overlap.

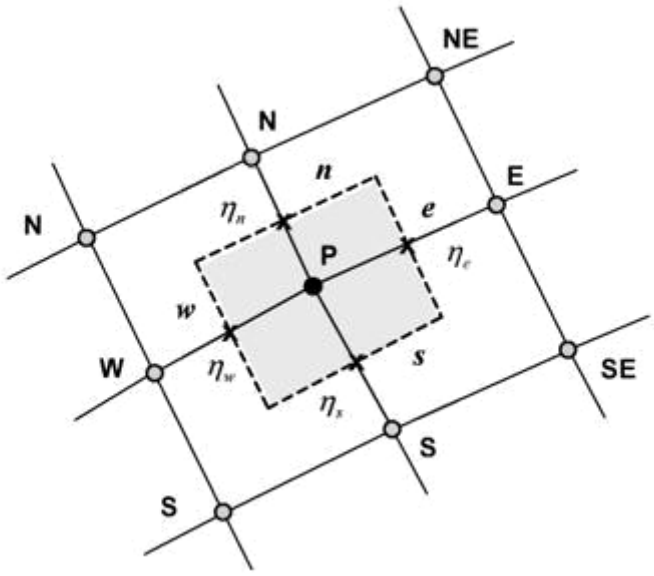

Figure 2.2: 2D Control Volume, from www.scielo.br

As seen in Equation (2.17), the transient and the source terms of the transport equation require a volumetric integration. One way to achieve second-order accuracy is to approximate these integrals as the product of the volumetric mean value with the volume of the cell, with the mean value being the value at the cell centre, such that

$$Q_P = \int_{\Delta V} q\, dV = \overline{q}\, \Delta V \approx q_P\, \Delta V \,. \tag{2.19}$$

This approximation is exact as long as the quantity *q* is constant or varies linearly within the considered CV.

The approximations of the surface integrals occurring in Equation (2.18) require the determination of the values at the cell faces to compute the corresponding fluxes. There are several numerical schemes available for this task. These schemes are generally based on the discrete solution of a one-dimensional advection equation of some scalar quantity *f* written as

$$\frac{\partial f}{\partial t} + u\frac{\partial f}{\partial x} = 0. \tag{2.20}$$

The so called first-order upwind scheme computes the advective fluxes across the faces using the node value immediately upstream, such that Equation (2.20) becomes

$$f_i^{n+1} = f_i^n - u\frac{\Delta t}{\Delta x}(f_i^n - f_{i-1}^n) \qquad \textit{for } u > 0, \tag{2.21}$$

where f_i^{n+1} is the value of the quantity *f* in the cell *i* at the iteration/time step *n+1*, *u* the advection velocity (assumed here as constant), Δt the time step and Δx the length of the computational cell. If the Courant number (named after Richard Courant) is

$$C = \left| u\frac{\Delta t}{\Delta x} \right| \leq 1, \tag{2.22}$$

this scheme is stable.

The second-order upwind scheme applies a Taylor series expansion of the cell-centered solution into the upstream direction such that the face value can be generally written as

$$\phi_f = \phi + \nabla\phi \cdot \vec{r}, \tag{2.23}$$

where $\vec{r}$ is the distance vector from the upstream cell centroid to the face centroid and the gradient $\nabla\phi$ is obtained from a Green-Gauss Node-Based Gradient Evaluation.

The Power-Law Scheme uses the exact solution of a one-dimensional advection-diffusion equation to interpolate the face value of the transported scalar.

The third-order MUSCLE Scheme is a modified version of the original Monotone Upstream-Centered Scheme for Conservation Laws (MUSCL) which applies piecewise

linear approximations using left and right extrapolated states. The scheme is constructed by blending a central differencing scheme with a second-order upwind scheme.

In the present simulations a second-order upwind scheme as implemented in FLUENT is used for all transport equations except for the transport of the volume fraction and the pressure interpolation equation.

For the advective transport of the volume fraction, the Geometric Reconstruction Scheme is applied. In the geometric reconstruction approach the interface is approximated by a piecewise-linear contour. The interface is assumed as a line (in 2D), or a plane (in 3D) within each cell. The general procedure is to calculate the position of the linear interface relative to the control volume centre. The second step is the calculation of the flux through each face. Finally, the volume fraction is updated using the balance of fluxes. The piecewise-linear representation of the interface is exemplarily shown in Figure 2.3. The numerical description of the interface obtained with a Donor-Acceptor Scheme is shown for comparison as well.

The donor-acceptor approach indentifies one cell as a donor of an amount of the considered fluid phase, and another neighbouring cell as the acceptor of the same amount of fluid. The fluid flux is limited by the occupied volume in the donor cell as well as the available free volume in the acceptor cell.

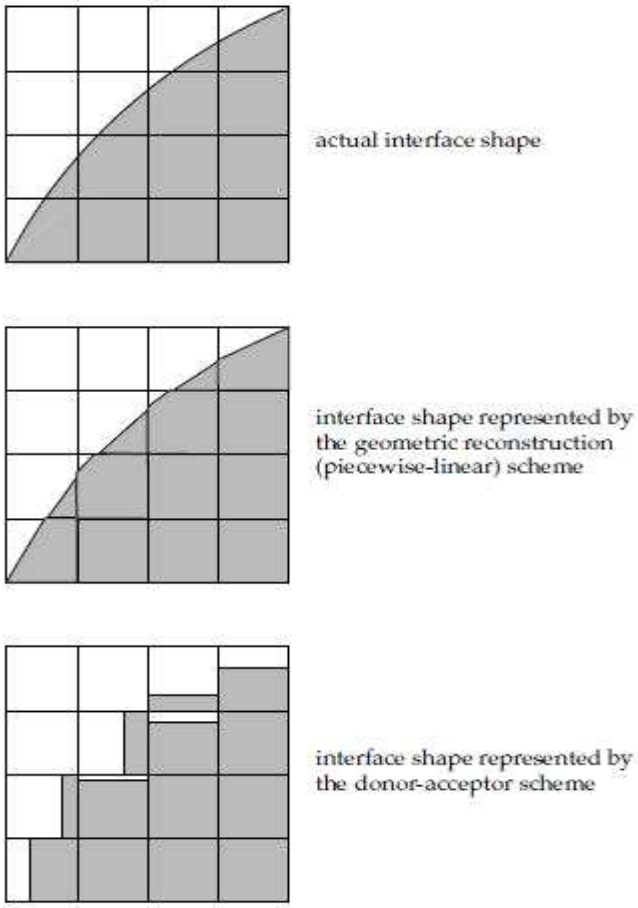

Figure 2.3: Interface approximation, from FLUENT User's Guide (2006)

2.2.2 Interpolation of the pressure

In the Finite-Volume method as implemented in FLUENT, the pressure as well as the velocities are by default stored at the centre of the control volume. The pressure correction requires the interpolation of the pressure onto the cell faces. As this interpolation may cause instabilities in case of high pressure gradients, the PRESTO scheme is used in the present simulations.

In the PRESTO Scheme the discrete continuity balance is applied to a "staggered" control volume about the cell face to compute the pressure directly at the face and no interpolation is needed.

2.2.3 Time discretization

Time dependent simulations require the integration of the differential equations over a time step Δt. An implicit time discretization scheme was applied in the presently considered problem. A first- and second-order accurate discretization of the transient term in

$$\frac{\partial \phi}{\partial t} = F(\phi) \tag{2.24}$$

is exemplarily shown by the following expressions, respectively:

$$\frac{\phi^{n+1} - \phi^{n}}{\Delta t} = F(\phi), \tag{2.25}$$

$$\frac{3\phi^{n+1} - 4\phi^{n} + \phi^{n-1}}{2\Delta t} = F(\phi). \tag{2.26}$$

Here, *n+1* identifies the value at the new time level, $t+\Delta t$, *n* the value at the current and *n-1* at the previous time level. *F* comprises all flux and source terms.

The implicit time integration evaluates the term on RHS using the values at the new time level *n+1*, such that

$$\phi^{n+1} = \phi^{n} + \Delta t\, F\left(\phi^{n+1}\right). \tag{2.27}$$

It has the advantage to be unconditionally stable with respect to time step size. Using the implicit time integration for the advective fluxes, the Finite-Volume discretized equation for the volume fraction reads

$$\frac{\alpha_q^{n+1}\rho_q^{n+1} - \alpha_q^{n}\rho_q^{n}}{\Delta t} V + \sum_f \left(\rho_q^{n+1} U_f^{n+1} \alpha_{q,f}^{n+1}\right) = \left[S_{\alpha_q} + \sum_{p=1}^{n} \left(\dot{m}_{pq} - \dot{m}_{qp}\right)\right] V, \tag{2.28}$$

where *n+1* is the index for the new time level, *n* for the previous time level. The face values $\alpha_{q,f}$ of the q^{th} volume fraction are computed using the Geometric Reconstruction approach as mentioned above. U_f is the face normal velocity based on the volumemetric flux across the face.

2.2.3.1 Pressure-velocity coupling

A pressure-velocity coupling scheme is required to solve the incompressible Navier-Stokes equations, where the pressure field is obtained by enforcing the continuity equation in the so called pressure-correction procedure. After applying the pressure correction the obtained velocity field satisfies the continuity equation.

As noted above in section 2.2.2, a PRESTO scheme is used. This implies that the pressure correction applies the continuity constraint on a staggered grid, where pressure is computed at the cell faces. If a colocated grid were used, the pressure correction can produce decoupled solutions with oscillating pressure leading to instability. Using a staggered grid with the scalars (ρ, p, η) located in the cell centres and the velocities located at the cell faces offers the advantages that the calculation of the pressure gradient and diffusion terms in the momentum equation require no interpolation. A staggered two-dimensional grid configuration is shown in Figure 2.4, where u and w denote the horizontal and vertical velocity components, and $\sum$, p, T the scalars.

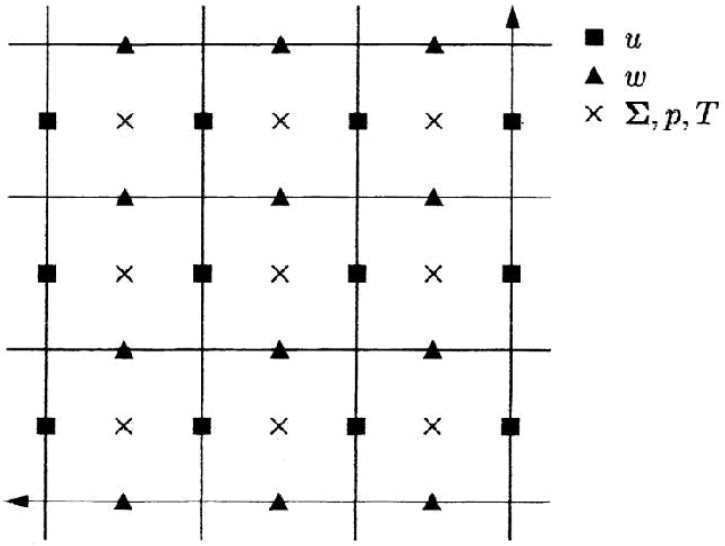

Figure 2.4: Staggered grid, from www.emeraldinsight.com

The pressure-velocity coupling involves the solution of a system of linear equations for the pressure. A PISO scheme is used for this task. PISO is a member of the SIMPLE family of pressure solvers, which achieves a high accuracy in satisfying the continuity equation by applying additional correction steps as compared to the classical SIMPLE method.

Chapter 3 – Methodology

3.1 Set up of the problem configuration

The computational domain (Figure 3.1) is axially symmetric with a radial extension *x/D=7*, and an axial extension *y/D=5.3*, where *D* denotes the droplet diameter. The droplet diameter was assumed to be *D=3.4mm* for all simulations. The bottom boundary is defined as a solid wall associated with a no-slip condition. At the y-axis being the axis of symmetry von Neumann boundary conditions are imposed. The upper boundary at $y=y_{max}$ is defined as pressure inlet, while the curved boundary to the right is defined as pressure outlet. Possible inflows at the permeable pressure inlet/outlet boundaries are specified as pure air.

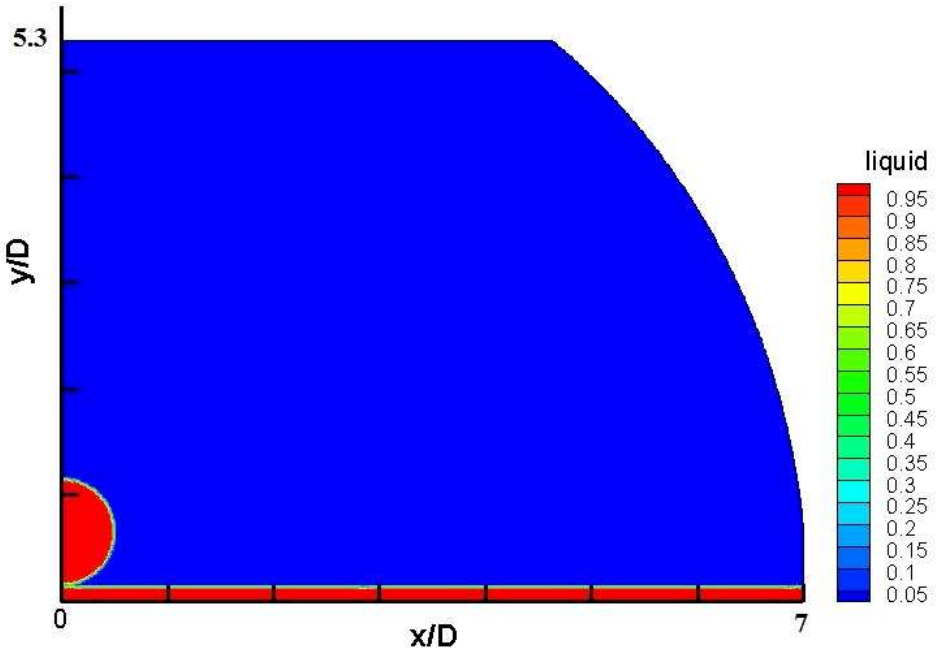

Figure 3.1: Total computational domain, with contours of the liquid volumetric volume fraction at the initial state

Figure 3.2 shows in more detail the contours of the liquid volume fraction at the initial state. The shown initial conditions basically apply to all considered cases, except for the liquid film at the bottom which does not exist in the cases with impingement on a dry surface. The colour map displayed in the contour plot in Figure 3.1 applies to all contour plots of the liquid volume fraction in all the following figures as well. Accordingly, the pure liquid phase is always denoted by red, the pure gaseous phase by

blue. The initial conditions are prescribed using a User defined Function (UdF). A detailed description of the presently applied UDF can be found in Appendix A. In the considered cases different impact velocities V_0 on a liquid surface as well as on dry surfaces are simulated. Furthermore, we investigated the evolution of a drop impact on dry surfaces with different wettabilities by varying the contact angle between the liquid and the solid surface.

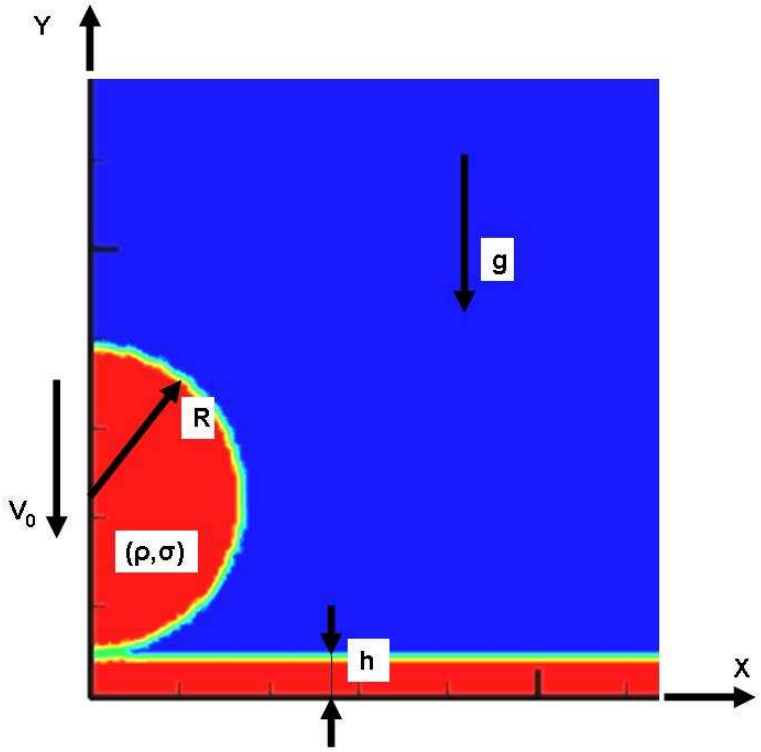

Figure 3.2: Contours of the liquid volumetric volume fraction at the initial state

The gaseous phase being ambient air was assumed as an ideal gas at standard pressure p_a=101325 Pa, while the liquid was considered as an incompressible medium. The surface tension was taken into account for all considered cases and was kept constant. The gravitational acceleration was also taken into account with a constant value of 9.81 m/s^2. The position of the fluid interface is associated with the liquid volume fraction having a value of α=0.5. The iso-contour with this value is visible as green line in Figure 3.2. Based on the evolution of the iso-contours at α=0.5 in time, the motion of the interface as well as the instantaneous local flow properties at the interface (e.g. velocities) are determined.

3.2 Grid generation

The meshing of the computational domain is one of the most important steps on the way to simulation results. Since the flow is assumed as axially symmetric, a two-dimensional grid has to be generated. In order to obtain a reasonable mesh, several aspects have to be taken into account, such as the required accuracy, the computational costs as well as special requirements relevant in the here considered cases. The GAMBIT version 2.4.6 was used as meshing tool.

Commonly, we can expect a smaller error of discretization for a finer mesh. Computational costs limit the number of cells available for domain discretization. Several things can be done to obtain a high mesh quality, while the computational costs stay within reasonable limits. For multiphase flows the interface is of highest interest. Therefore, regions with gas-liquid interfaces should already be resolved by an adequate grid at the initialization stage in order to capture the exact initial position of the interface.

Due to the propagation of the liquid/air interface, a fine mesh is basically needed for the most part of the domain. To increase computational efficiency, a dynamic grid adaption in the regions near the interface can be performed. The task of a dynamic grid adaptation is to refine the grid in regions where high resolution is needed, and to coarsen it, where low spatial resolution is needed.

An extremely refined grid near the interface generally leads to very sharp gradients in the flow variables. These may finally cause numerical difficulties due to divergent solutions in the pressure-velocity coupling. Therefore, the mesh generation has to aim at a good compromise between an adequate resolution and a stable simulation.

The first attempt was to create an adequate grid for use in combination with dynamic grid adaptation. The position of interest for a dynamic refinement is the interface between the liquid and the ambient air. The phase gradient has been used for tracking the interface. In order to obtain an adequate resolution at the initialization stage, the grid is refined in zones, where the interface between liquid and the ambient air is located. The grid consists of triangular and rectangular cells. Investigations on different grids with different cell shapes have shown that triangular cells capture the interface better

than rectangular cells and are therefore used for areas, where the interface will expectedly propagate.

Using a dynamical grid adaptation finally turned out to be unfeasible due to the appearance of numerical noise. The problems related to this issue are discussed in more detail in section 4.

Applying instead a constant uniform mesh resolution as shown in Figure 3.3, avoided the problem of numerical noise as compared to the dynamical grid adaptation. It was therefore used for all cases with wetted surfaces. A grid convergence study was done with the focus on the effect of different grid resolutions on the radial position on the moving crown. The results of this grid sensitivity study are presented in section 4.

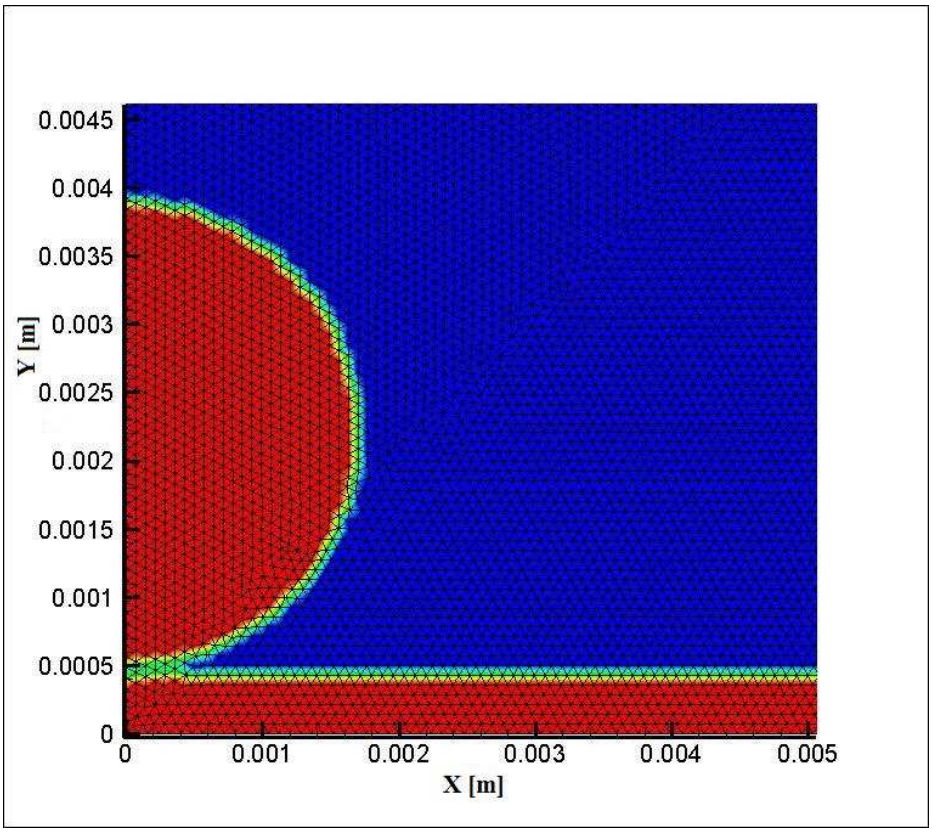

Figure 3.3: Drop area after the initialization, uniform mesh

A different, but still not dynamically adapted, grid was generated for the impact on dry surfaces consisting of two areas with different grid resolution. As such, the grid

distinguishes a highly resolved zone including the region close to the wall and the region which is initially occupied by the drop. This refined zone exhibits a uniform resolution like the uniform mesh for the impact on wetted surface. The remaining region of the domain is discretized using a much coarser mesh applying a growth function for the cell size (see Figure 3.4).

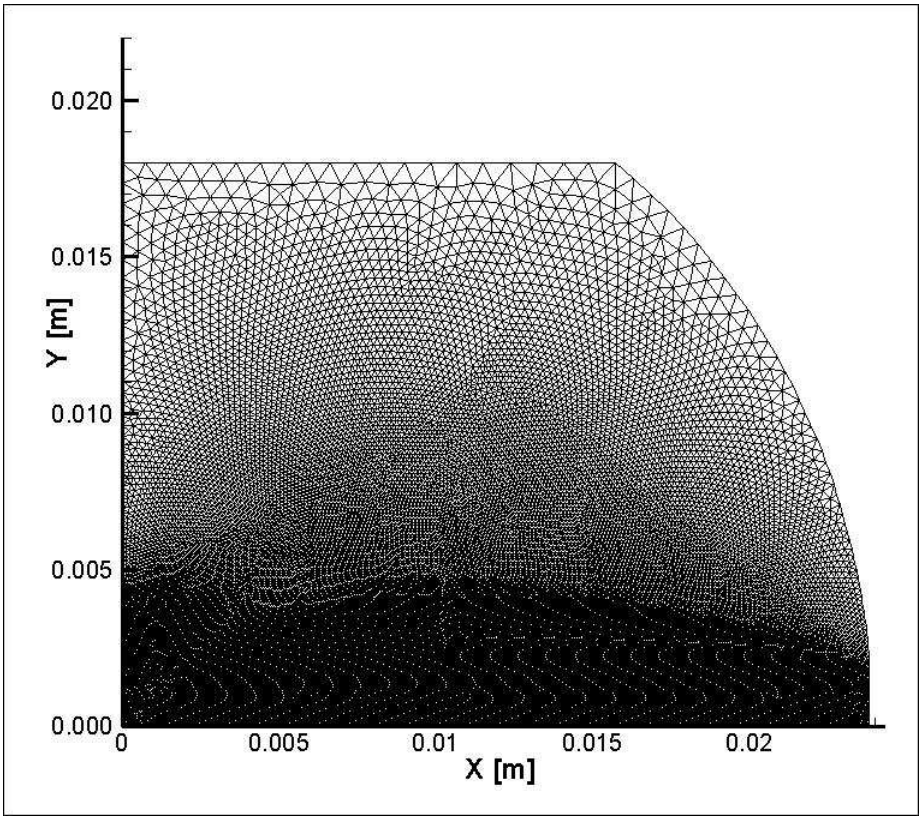

Figure 3.4: Grid for the drop impact on dry surfaces

3.3 General parameter setting

This section gives an overview of those parameters, which were equally applied in all cases. The case-to-case dependent individually selected parameters will be addressed in the discussion of the respective case. Further details on the FLUENT settings for the considered cases are given in the Appendix.

General parameter setting in FLUENT
► Pressure based solver in implicit formulation
► First order implicit time formulation
► Green-Gauss node based gradient option
► Absolute velocity formulation
► Volume of Fluid multiphase model, implicit scheme with Courant number = 0.1, with implicit body force formulation
► Laminar viscous model
► Default air properties with ideal-gas law
► depending on the case default ethanol liquid (C2H5OH) or water liquid (H2O)
► Liquid as primary phase and air as secondary case, constant surface tension between the phases (Ethanol: 22.39 E-03 N/m; Water: 7.28 E-02 N/m) for cases with dry surface the “wall adhesion” enabled
► 101325 Pa operating pressure, reference pressure location at (x; y)=(0.001; 0.017), gravitational acceleration = -9.81 m/s^2, operating temperature: 288.16 K, specified operating density enabled with 1.225 kg/m^3
► Solution Controls: PISO pressure-velocity coupling; discretization: PRESTO for pressure; second-order upwind for density and momentum; Geo-Reconstruct for the volume fraction equation
► the residuals convergence criteria for continuity and velocities is 1E-04
► the iteration process operated with variable time step, the starting time step size depended on the case and was from 1E-05 sec to 1E-07 sec, the global Courant number is not constant for all cases

Chapter 4 – Results and analysis

4.1 Grid sensitivity study

Several test simulations were carried out applying a dynamic grid adaptation. The dynamic adaptation was repeatedly performed at the beginning of each run and after a specified number of time steps. The local value of the local gradients of the volume fraction was used as criterion for local refinement or coarsening. The grid refinement appeared to work reasonably well, while the coarsening lead to numerical problems. Further investigations using the local velocity gradient as refinement/coarsening criterion lead to the same problems.

In summary, the dynamic grid adaption exhibited two main shortcomings. The first is associated with the occurrence of numerical noise visible as small dispersed liquid spots in the gaseous region as shown in Figure 4.1. These tiny droplets did not originate from the continuous liquid phase. The occurrence of such artificial droplets was mainly observed in regions near the interfaces, and in regions which were previously occupied by liquid. It is also seen form Figure 4.1, that the numerical noise causing the formation of unphysical tiny liquid spots in turn leads to an unfeasible further local grid refinement. Secondly, a subsequent refinement of the grid strongly increases the grid size leading to unacceptably high computational costs. Therefore, the option of dynamic grid adaptation was discarded, and all simulations were carried out on a constant grid. As mentioned in the previous chapter, a triangular uniform mesh was the final choice. In particular, the grid near the wall was finer for the impact on dry surface to resolve the contact region. A comprehensive grid sensitivity study was performed to finally decide on the most appropriate grid. Four different meshes as shown in Table 4.1 were examined. The impact velocity of the drop was always assumed V_0=1.23m/s. The thickness of the pre-existing wall film was set h_0=0.43mm.

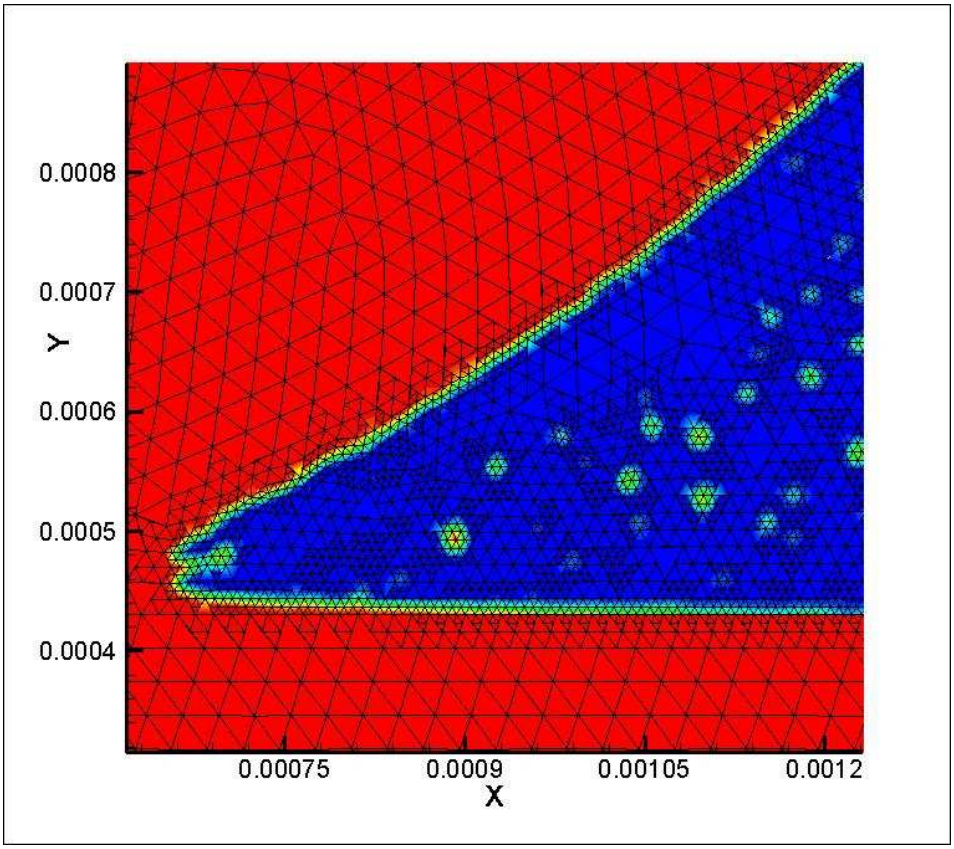

Figure 4.1: Adaptive grid refinement at the interface and numerical noise

Grid	Number of cells
Mesh 1	87 100
Mesh 2	137 700
Mesh 3	177 900
Mesh 4	206 300

Table 4.1: Meshes used for the grid sensitivity study

The simulation with the finest mesh, Mesh 4, caused high computational costs as well as numerical instabilities, and was therefore aborted.

Figure 4.2 shows the instantaneous contours of the liquid volume fraction at a certain time t as obtained with the first three different meshes, listed in Table 4.1. The radially extending liquid crown has almost the same shape for all grids. Some grid dependence can be observed only in the deformation of the tip of the crown and in the formation of secondary droplets. The better resolution leads obviously to a somewhat different breakup of the liquid rim into secondary droplets.

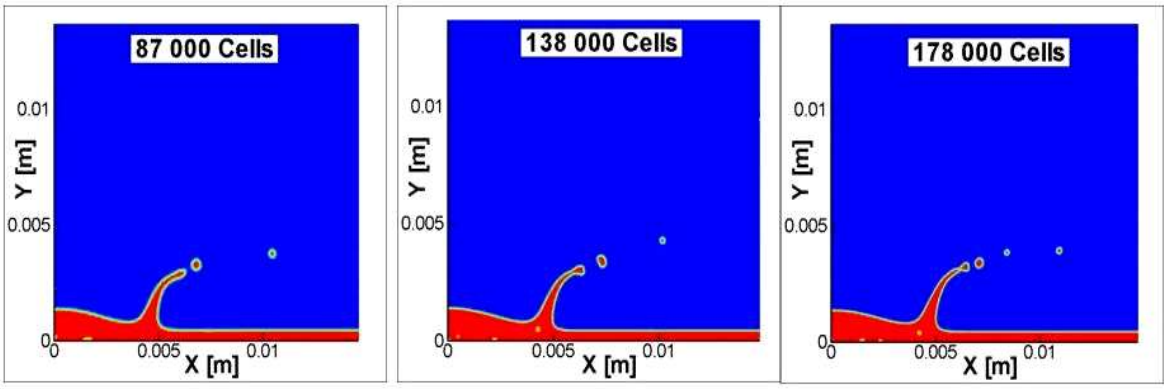

Figure 4.2: Contours of liquid volume fraction on different meshes (t=0.0031sec)

The formation of secondary droplets is also visible in the radial expansion of the crown tip plotted over the time as shown in Figure 4.3. The break-off of secondary droplets from the tip is indicated there by the edges in the curves.

Besides this difference in the prediction of the breakup into secondary droplets, the individual curves show on the average no significant grid dependence. Indeed, the curve of the finest grid lies between the two coarser ones.

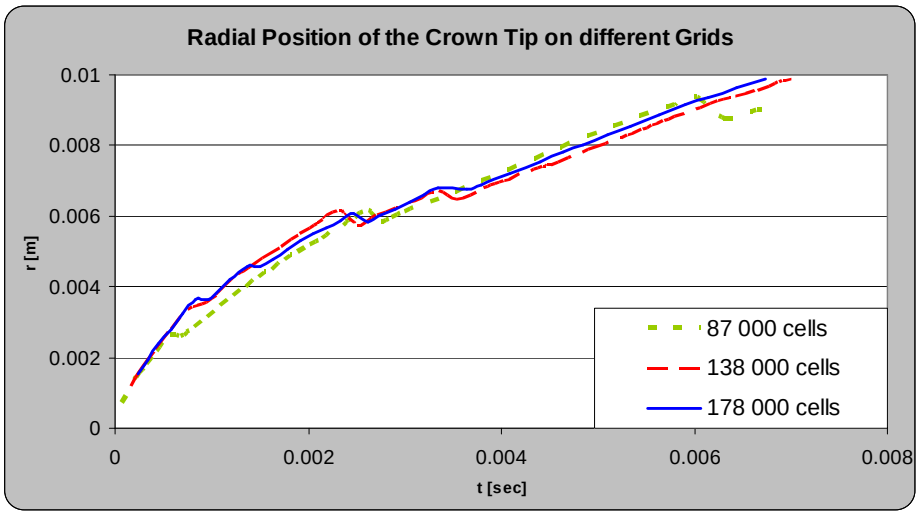

Figure 4.3: Radial position of the crown tip on different grids

Although the finest mesh was found to capture the sharpness of the interface best, Mesh 2 was the final choice. This grid provided a good resolution of the essential flow features at the interface like the motion of the crown, and it was found to be reliable concerning the stability of the simulations. The creation of more or less secondary droplets was not used as decisive criterion here. Physically speaking, the breakup of the rim of the crown is strongly influenced by perturbations into the circumferential direction, which are not captured by any grid due to the assumption of axial symmetry.

4.2 Drop impact on wetted surfaces

In total three cases were considered here. The liquid of the drop and the surface film was specified as Ethanol (C_2H_5OH) with a constant surface tension of 22.39E-03 N/m, Density ρ=790kg/m^3 and dynamical viscosity η=0.0012 kg/ms for all three cases. The thickness of the pre-existing liquid film on the surface was always chosen to be 0.43 mm. The drop diameter was always set to 3.4mm.

The characteristic parameters of the considered cases in cases of the impact on wetted surfaces are listed in Table 4.2. The actually imposed parameter setting is essentially guided by two aspects: first, the simulations should cover the splash as well as the non-splash regime. Secondly, the flow conditions should resemble the conditions of the simulations of Weiss and Yarin (1999), so that their results can be used for a comparison with the present simulations. Weiss and Yarin (1999) solved the evolution of the interface using a boundary-integral method neglecting viscous forces. In accordance with their work the same non-dimensionalization of the time and velocity, $T_{WY}=t\cdot\sqrt{(g/R)}$ and $U_{WY}=u/\sqrt{(g\cdot R)}$, respectively, are used in the present section. Based on experimental observations Cossali *et al*. (1997) derived a correlation for the critical value of $K=K_{crit}$ written as

$$K = Oh^{-2/5}\cdot We = 2100 + 5880\cdot H^{1.44}, \qquad (4.1)$$

which demarcates the transition from the no-splash to the splash regime. With the present non-dimensional film height of $H=h/D$=0.125. Equation (4.1) gives K_{crit}=2399. According to this empirical correlation only case_c in Table 4.2 is clearly above this limit, so that only case_c should feature a splash.

Case	Impact velocity	*We* number	*Re* number	*Oh* number	*K*
case_a	0.1 m/s U_{WY}=0.77	1.2	224	4.89 E-03	10
case_b	1.3 m/s U_{WY}=10	203	2910	4.89 E-03	1704
case_c	2.6 m/s U_{WY}=20.1	811	5820	4.89 E-03	6810

Table 4.2: Case data for drop impact on wetted surface

Figure 4.4 presents a qualitative overview of the computational results displaying the contours of the liquid volume fraction at different dimensionless times T_{WY}. As expected from the splashing criterion based on Equation (4.1) we obtain no splashing for case_a. The impact of the drop generates a bulky wave moving radially outwards. The impact velocity is evidently not high enough to provide enough momentum for the creation of a liquid finger at the front of the propagating wave. Subfigure We=1.2 / T_{WY}=5.2 shows a non-wetted area at the centre. The liquid film evidently breaks up and forms an inner rim due to the action of the surface tension. The splashing criterion based on Equation (4.1) is not reflected in case_b, as it can be seen from the formation of a crown, typical for a splash. Besides the inaccuracies and model errors, which inherently occur in any discretized numerical computations, the observed discrepancy could be partly due to the fact that the parameter K associated with case_b is not far below the critical value. At the same time the critical value obtained from the correlation (4.1) can certainly not be regarded as a sharp demarcation point between no splash and splash, so that splash may occur at somewhat lower values of K_{crit}. A splash can be observed for case_c, as it is expected from Equation (4.1).

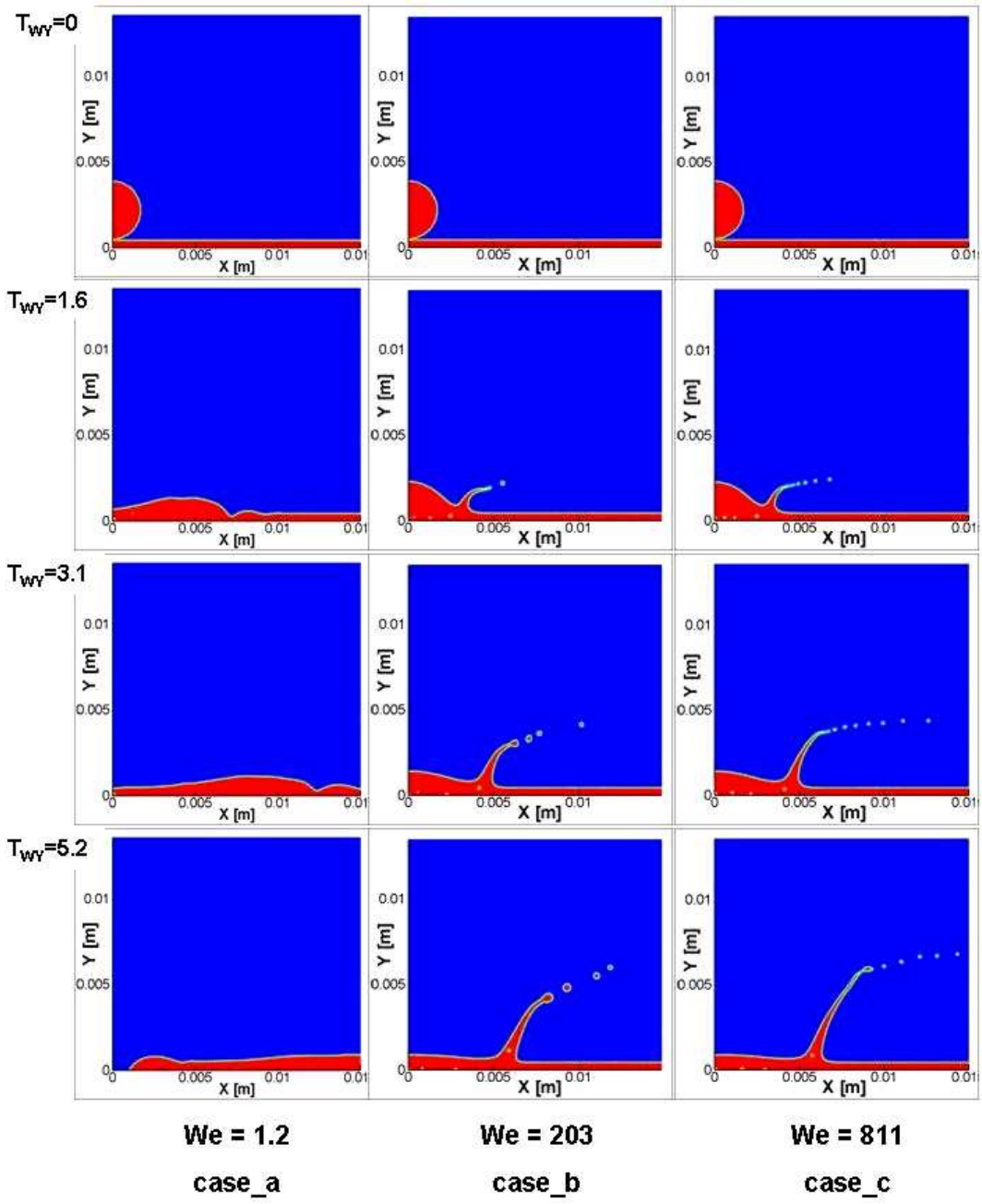

Figure 4.4: Contours of liquid volume fraction at different non-dimensional times, T_{WY} for case_a, case_b and case_c

As seen from a comparison of the right two columns, the temporal evolution of the splashing process is similar in case_b and case_c associated with *We*=203 and *We*=811, respectively. On the top of the expanding crown a rim is formed which is finally the origin for the secondary droplets. The reasons for this break up are mainly the Plateau-Rayleigh instability as well as local velocity differences. The Plateau-Rayleigh instability is due to the tendency of a liquid to minimize its surface area, hence to

assume a lower energetic state. The instability which finally leads to a breakup into a secondary drop is triggered by perturbations in the liquid stream. For the higher impact velocity in case_c the liquid rim is thinner and protrudes higher into the ambient air. As a consequence, more and smaller secondary droplets are generated. Note that the first secondary droplet already left the domain in subplot for We=811 and T_{WY}=5.2, which indicates a higher radial velocity of the secondary droplets in this case.

None of the figures show a generation of capillary waves, preceding the crown.

Now we take a closer look at the shape and the propagation of the crown compared against the results of Weiss and Yarin (1999), who considered in their simulations cases with the same non-dimensional film thickness H and very similar Weber numbers We. Figures 4.5 a, b show a sequence of interface contours, where the radial extensions of the crown (measured at the outer wall of the vertical lamella) are the same in both simulations. In the result of Weiss and Yarin (1999) the crown is first tilted inwards. Later, it is tilted slightly forwards and propagates without significant change in shape. No secondary droplets are generated as liquid breakup cannot be reproduced by their solution method. In contrast, the present results feature a more physical behaviour as observed in experiments. The crown is always tilted forwards, the upwards ejected lamella gets thinner and higher during the expansion, and secondary droplets are generated. With respect to the predictions of these typical features of a splash, the present results are in better agreement with the results from a previous simulation by Rieber and Frohn (1999). This can be exemplarily seen from Figure 4.6, where the evolution of the interface obtained for roughly the same non-dimensional film height H=0.116 but a higher Weber number We=598 shows essentially a very similar behaviour to the present results displayed in Figure 4.5 b.

Estimating the propagation speed of the crown from the instantaneous moments of time T_{WY} associated with the individual radial positions shown in Figure 4.5 a, b gives a roughly 10% higher level for the present results. The retarding effect of viscosity, which is accounted in the present simulations in contrast to the inviscid simulations of Weiss and Yarin (1999), does evidently not play an important role. Its neglect appears therefore as justifiable.

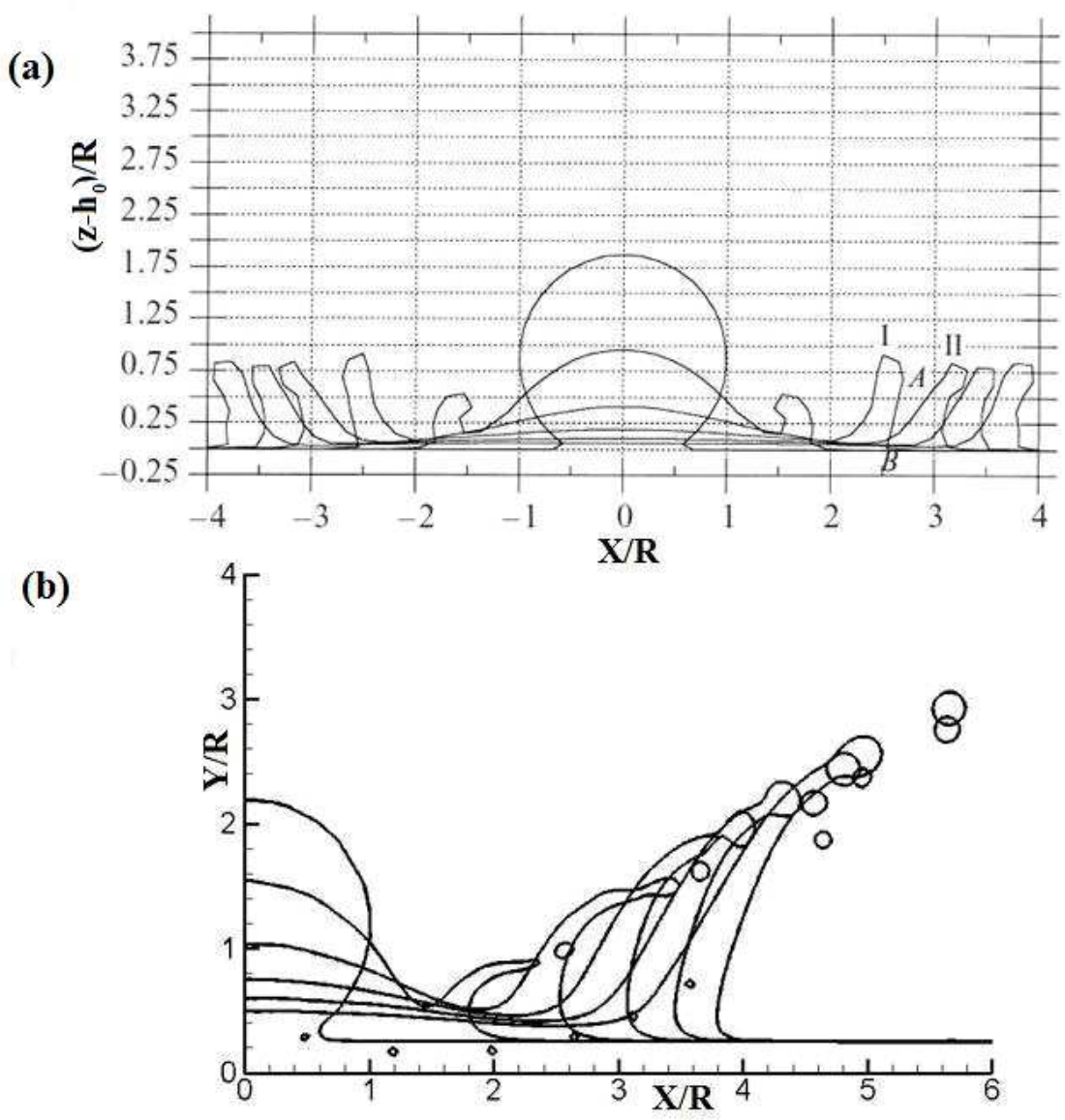

Figure 4.5: Evolution of the free surface in case of *We* = 203, (a) shows the simulation result of Weiss and Yarin (1999) at non-dimensional times T_{WY}=0, 0.1, 0.2, 0.3, 0.4 and 0.5. (b) shows the present simulation results for case_b with *We*=203 at non-dimensional times T_{WY}=0, 0.08, 0.17, 0.25, 0.33 and 0.41

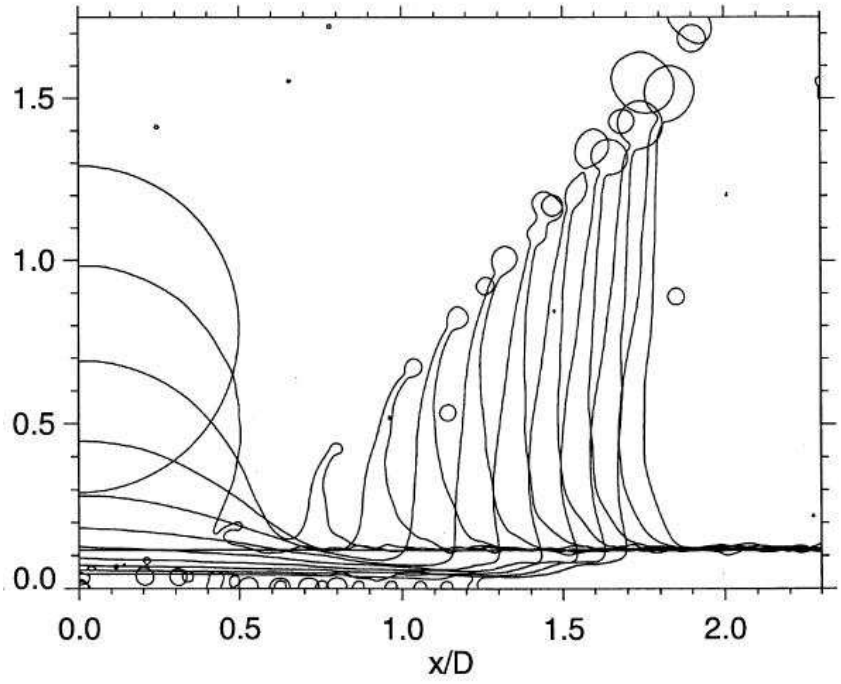

Figure 4.6: Evolution of the free surface, from Rieber and Frohn (1999)

The temporal variation of the position of the crown predicted in the present simulations follows reasonably well an analytical asymptotic solution obtained by Yarin and Weiss (1995), as seen from Figures 4.7 and 4.8. According to the shown analytical approach, the radial propagation of the crown base for a single impact on a thin pre-existing liquid layer can be estimated as

$$\frac{r_c}{D} = \left(\frac{2}{3}\right)^{1/4} \frac{V_0^{1/2}}{D^{1/4} h_0^{1/4}} (t - t_0)^{1/2}, \tag{4.2}$$

where r_c is the radial crown position, t is the time beginning from the moment of impact, and t_0 is some empirical time constant. This theoretical estimate assumes the liquid as incompressible, and it is limited by the condition

$$K = We \cdot Oh^{-2/5} >> 1, \tag{4.3}$$

which implies a negligibly small effect of surface tension. The condition is satisfied for case_b and case_c. The instantaneous radial positions of the propagating crown are measured at the outer wall of the liquid sheet emanating from the base of the crown. The fact that the analytical curve increasingly exceeds our simulation results is not surprising. As responsible reasons for this deviation can be found in the exclusion of the

effect of surface tension, ambient pressure and viscous forces, which may all become increasingly relevant as time proceeds.

The evident deviation from the analytical results is in well in line with the findings of Yarin (2006). He compared the analytical theory with a best fit curve of various experimental data and observed pretty much the same discrepancy.

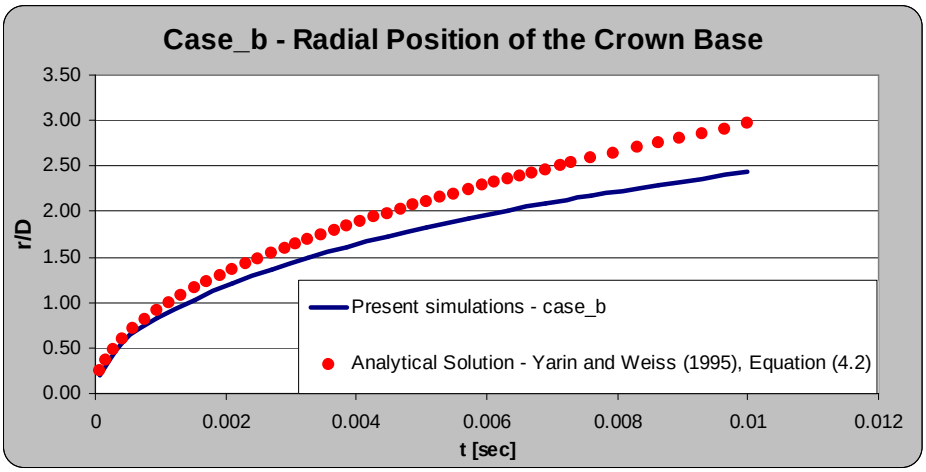

Figure 4.7: Comparison of numerical against analytical result for case_b

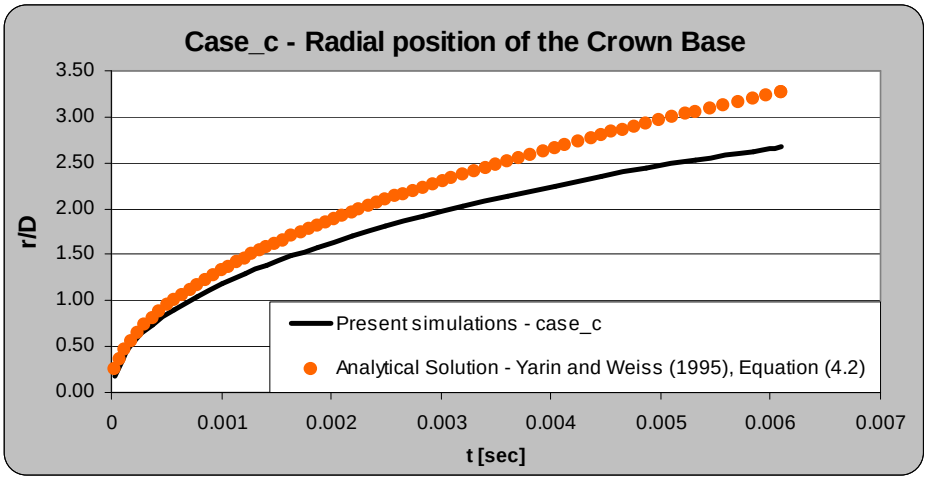

Figure 4.8: Comparison of numerical against analytical result for case_c

Another interesting phenomenon is reproduced by the present simulations as well. Immediately after the impact of the drop on the film the velocity inside the liquid near the wall changes almost step like from the impact value to zero. As seen from Figure

4.9 a, this leads to a peak in the static pressure in the neck between the drop and the film. The pressure peak causes an ejection of liquid into the horizontal direction as seen from the contour line of the interface in Figure 4.9 b. This phenomenon termed as "jetting" is hardly accessible in experiments, but it could be observed in the simulation results of Weiss and Yarin (1999), and of Josserand and Zaleski (2003) as well. A neck propagation with jetting as exemplarily shown in Figure 4.10 for case_b requires however sufficiently high impact velocities. Hence, no jetting occurs at small Weber numbers as in the present case_a.

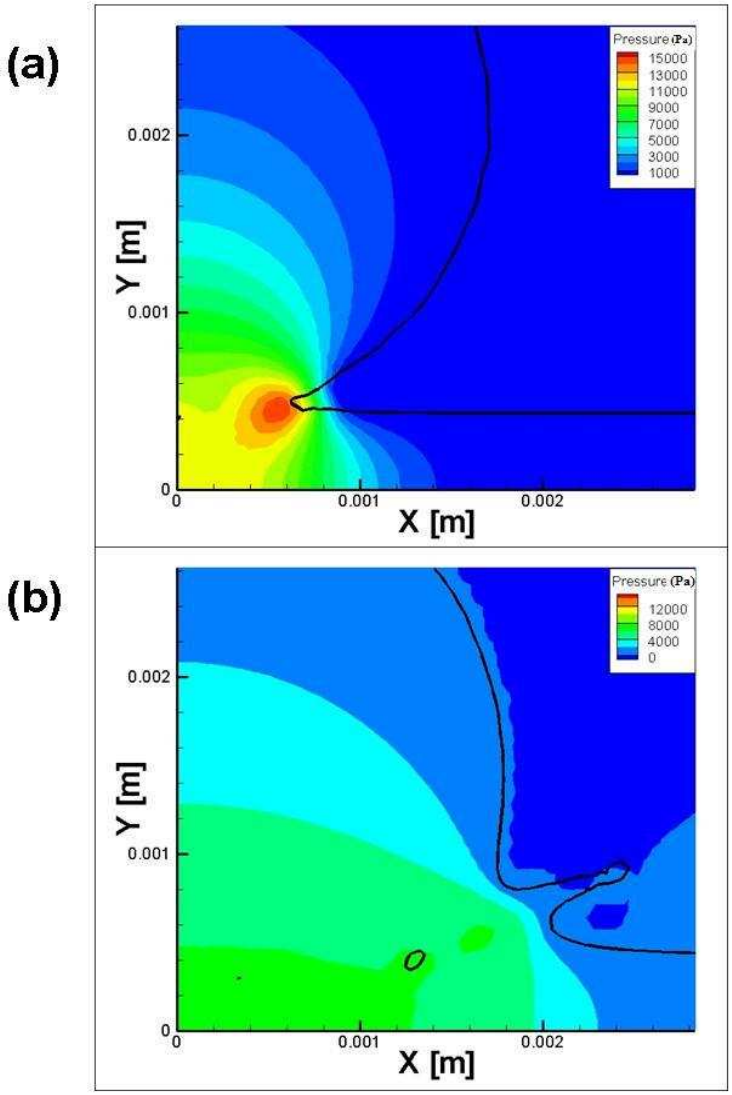

Figure 4.9: Static pressure field and contour of the interface, denoted by the black line shown for case_c at non-dimensional time T_{WY}=1.8e-3 and (b) T_{WY}=2.6e-3, respectively

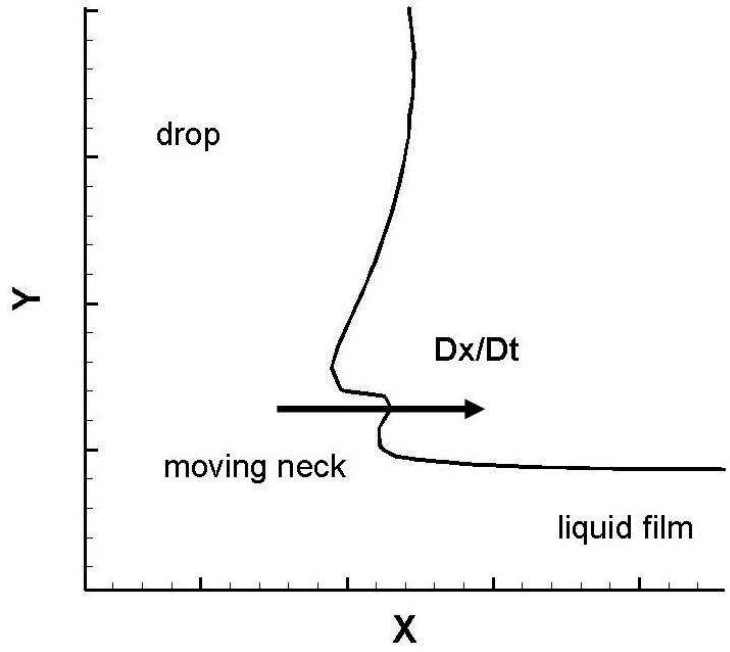

Figure 4.10: Shape of the moving neck with jetting, at non-dimensional time T_{WY}=0.016, case_b with *We*=203

The comparison of the propagation velocity of the neck at the critical stage shows a relatively high disagreement with the corresponding results of Weiss and Yarin (1999). As it is seen form Figure 4.11 displaying the velocities at corresponding radial position of the neck for the low Weber number case without jetting, the values differ by almost a factor of ten. The same tendency, although quantitatively less pronounced, is revealed in a high Weber number case with jetting when comparing the velocities of the tip of the horizontal jets obtained again at corresponding positions of the neck (see Figure 4.12). The observed discrepancies at the very early stage after the impact can be mostly attributed to the different initial conditions applied in the simulations. Weiss and Yarin (1999) started with a droplet which is already attached to the pre-existing film in order to ensure a continuous non-interrupted liquid-gas interface as required by their solution method. In contrast, the present simulations started with a drop completely detached from the surface of the film. Thus, it is not surprising that this difference may strongly affect the initial stage beginning with the very first contact of the drop liquid with the liquid of the film.

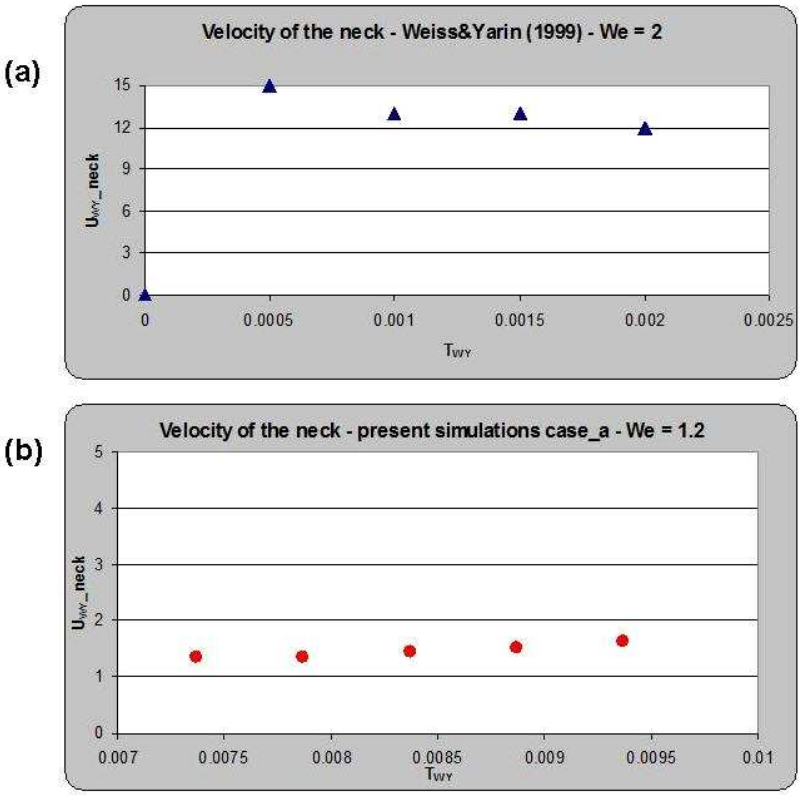

Figure 4.11: Comparison of the neck velocities for case_a

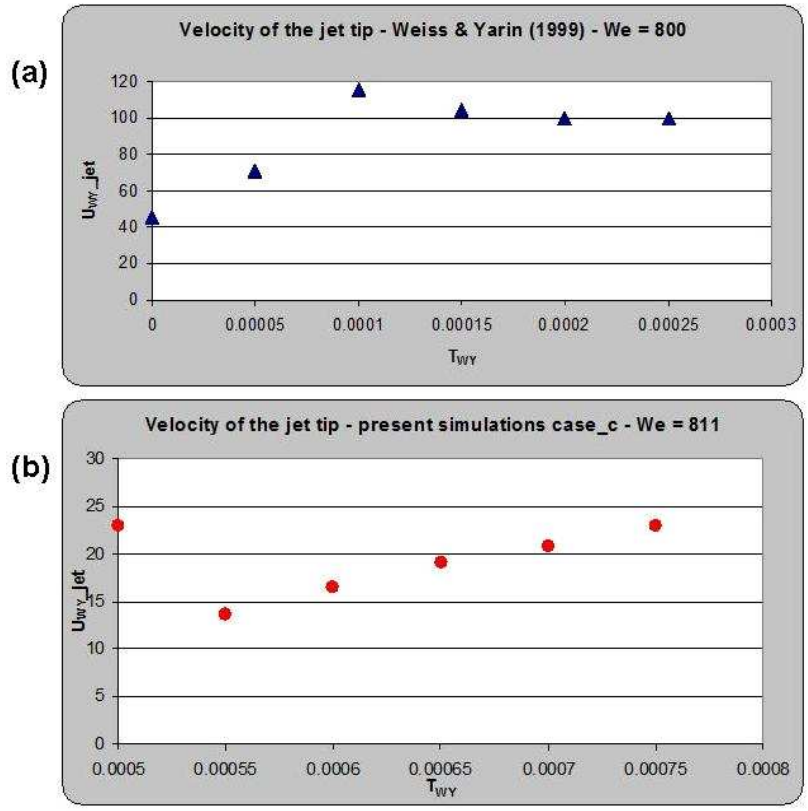

Figure 4.12: Comparison of the jet tip velocities for case_c

4.3 Drop impact on dry surfaces

In comparison to the impact of drops on liquid surfaces, the motion of the liquid following the impact on dry surfaces is additionally affected by the wettability of the solid surface. The surface wettability can be parameterized by the contact angle at the contact line between the liquid, air, and the solid surface. The contact angle varies between zero for the perfectly wetting (hydrophilic) case, and 180° for the perfectly non-wetting (hydrophobic) case.

Water (H_2O) was specified as the liquid for all simulations of drop impact on dry surfaces. We specified the following liquid properties: surface tension σ=7.28E-02 N/m, density ρ=998.2kg/m^3, and dynamic viscosity η=0.001003 kg/ms. The difference in the computational setup compared to the simulations of a drop impact on a liquid surface, lies mainly in the activation of a wall adhesion model prescribing a certain contact angle. Our numerical simulations are focused on the kinematic and spreading phase of the liquid. It is not possible to account the surface roughness in the wall adhesion model presently implemented in FLUENT. All quantities shown in the following section are non-dimensionalized using the impact velocity V_0 and the initial drop radius $R=D/2$ as reference scales. Accordingly, the non-dimensional time, spatial length, and velocity read $T = t \cdot \frac{V_0}{D}$, $X = \frac{x}{R}$, $U = \frac{u}{V_0}$, respectively.

The so called spread factor $d^* = \frac{r}{R}$ represents the ratio of the instantaneous radial expansion of the spreading liquid on the surface to the initial radius, and will be used for comparisons later on.

Table 4.3 lists the specific conditions of all simulated cases. Basically, the cases were specified to examine the influence of the contact angle on the flow behaviour with varying impact velocities. Accordingly, three different contact angles were specified in combination with two different impact velocities, associated with two different Weber and Reynolds numbers. Experimental data are hardly available for such a wide range of the contact angle. In order to have comparable experimental data we defined the conditions of some cases to match with the conditions considered in the experiments of Rioboo *et al*. (2002).

A well wetting surface associated with a contact angle of 10 degrees is assumed in the first two cases, listed in Table 4.3. This value of Θ refers to the advancing contact angle of water on glass. Such a case was also considered in the experiments by Rioboo *et al.* (2002).

As second contact angle we chose 75 degrees associated with case_dry_c and case_dry_d in Table 4.3. This value applies to surfaces which occur most frequently in technical applications. Generally, the value of Θ=90° is used to distinguish between hydrophilic and hydrophobic natural surfaces. With this respect the chosen value lies closely below this threshold.

The last two cases listed in Table 4.3 are associated with a contact angle being 170 degrees which represents a super hydrophobic surface. According to Kannan and Sivakumar (2008), hydrophobic surfaces show almost the same contact angle for spreading and receding. A typical example for a hydrophobic natural surface is the lotus leaf.

Case	D [mm]	V_0 [m/s]	*We*	*Re*	*Oh*	Θ [°]
Case_dry_a	2.77	1.12	48	3087	2.24 E-03	10
Case_dry_b	2.77	3.76	537	10365	2.23 E-03	10
Case_dry_c	3.04	1.18	58	3570	2.13 E-03	75
Case_dry_d	2.77	3.76	537	10365	2.236 E-03	75
Case_dry_e	2.77	1.22	48	3087	2.236 E-03	170
Case_dry_f	2.77	3.76	537	10365	2.236 E-03	170

Table 4.3: Case data for drop impact on dry surfaces

Figure 4.13 and Figure 4.14 presents a qualitative comparison of the simulated spreading of the liquid after the impact obtained for the low and higher Weber number cases with *We*≈50 and *We*=537, respectively. The contour plots show the propagation of the drop liquid on surfaces with different wettabilities at selected instants of non-dimensionalized time. Each column refers to the same contact angle.

The notable influence of the contact angle in case of low velocity impacts becomes obvious in Figure 4.13. The first column shows the spreading process on the highly wetting surface. The early emergence of a finger at the outer edge of the lamella for this case, visible at dimensionless time T=0.78, is surprising. Instead of the expected mainly surface bounded spreading, caused by the wall adhesion, we observe the generation of such a small ridge. As the ridge propagates outwards, the wall bounded liquid spreads increasingly faster such that the liquid ridge stays behind and flattens with time. The reason for this flow feature is found in the wall adhesion. It enhances the wall bounded radial propagation of the liquid as the effect of the inertial forces associated with the initial impact diminishes. As such, it has higher influence in cases of low velocity impacts. The comparison between the three columns in Figure 4.13 supports this reasoning, where we generally observe a wider radial expansion of the liquid sheet for smaller contact angles Θ. Thereby, an increasing influence of the surface tension is linked to the falling influence of the wall adhesion. In short, the higher the contact angle, the higher is the influence of the surface tension.

A further typical phenomenon occurring at increased contact angles is reproduced in a qualitative realistic manner as well. While the whole liquid mass always resides in a continuous lamella in case of Θ=10° and 75°, we observe the ejection of a secondary droplet in the case of the hydrophobic surface with Θ=170°. Indeed, this break up resembles a well known flow feature of a water drop impacting on a lotus leaf. After the ejection of a secondary drop (subfigure with Θ=170° at dimensionless time T=4.40) we can also observe the expected water repellent behaviour, indicated by the appearance of an unwetted region at the centre. The aggregation of the receding liquid leads to a bulging at the edges of the lamella. The observed phenomenon is also termed “viscous dewetting”, which typically occurs in the spreading of a viscous liquid on a hydrophobic surface with negligibly small inertial effects (de Gennes *et al.* (2004)).

As it is seen from Figure 4.14, referring to the cases with the higher Weber number, drop inertia has controlling influence to the flow behaviour of the spreading. The inertial forces induced by the initial momentum of the impacting drop have a significant influence on the spreading process.

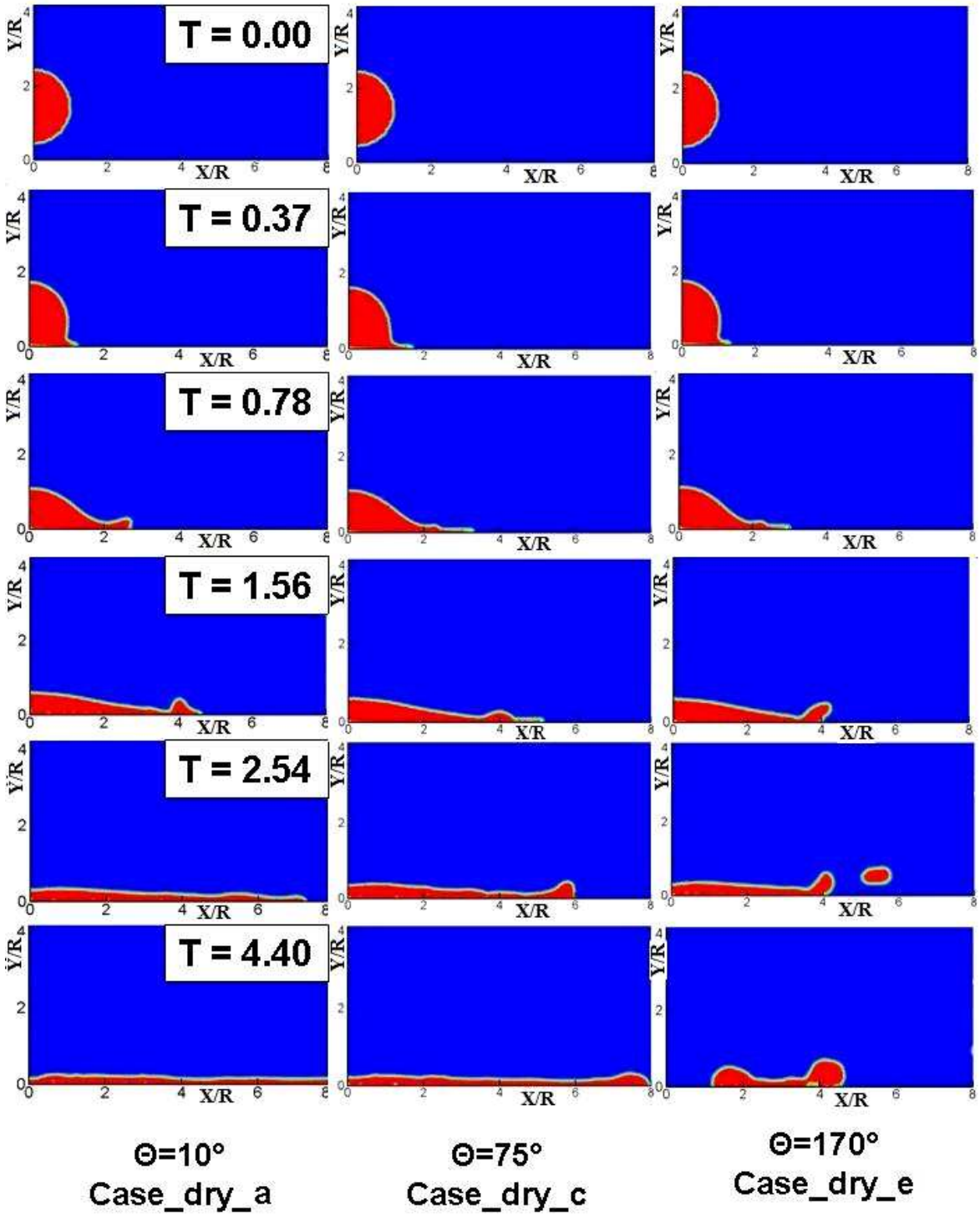

Figure 4.13: Contour plots of the cases with the low Weber number $We \approx 50$

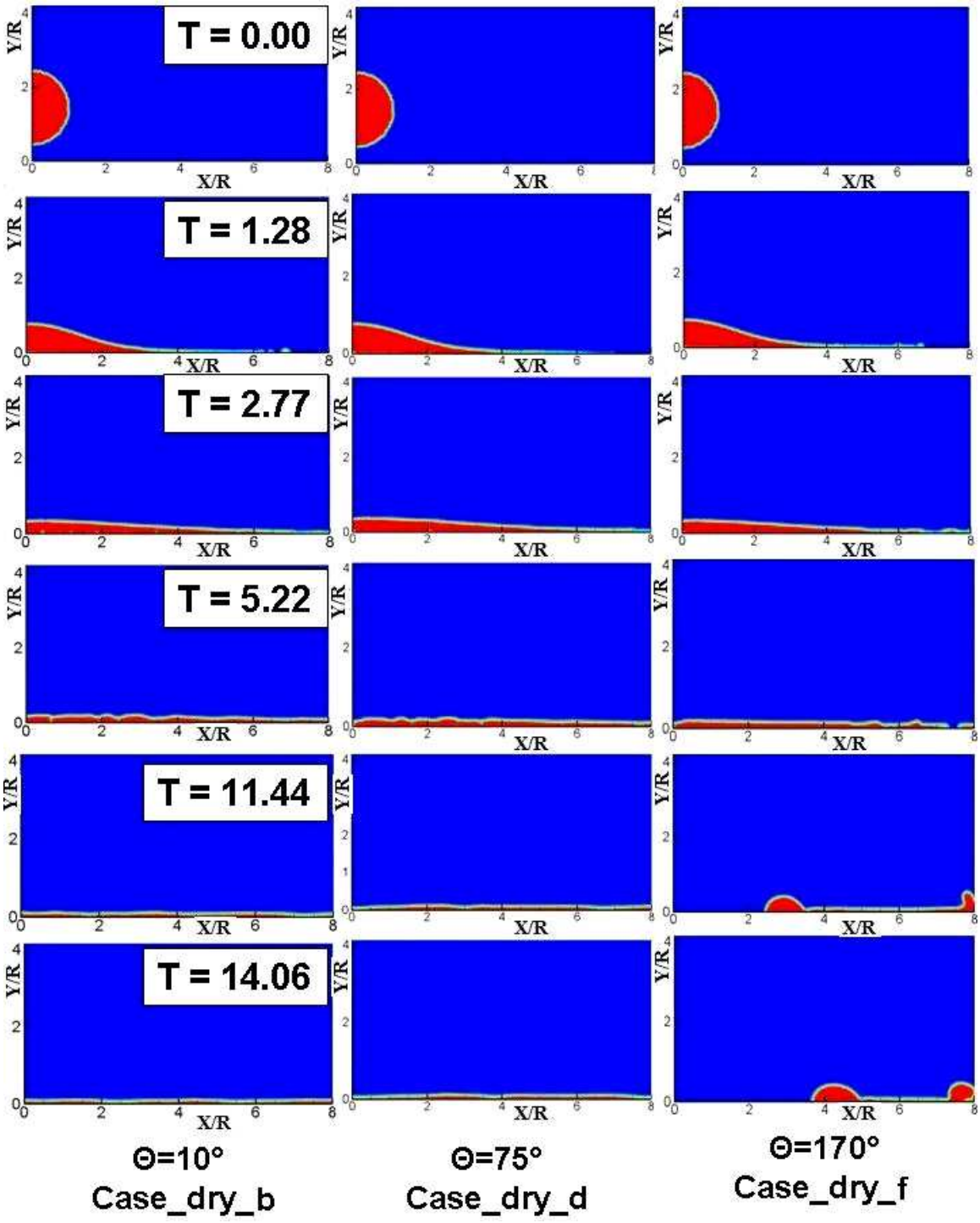

Figure 4.14: Contour plots of the cases with the high Weber number *We* = 537

In contrast to the cases with the low Weber number discussed above, most part of the spreading process is almost identical for all three considered wettabilities (Figure 4.14). So we can not clearly distinguish notable differences in the radial expansion of the liquid sheet displayed at the same earlier moments of time.

During the early stage the spreading of the liquid is obviously mainly driven by the inertial forces induced by the impact. The effects of the wall adhesion and surface tension become visible at the later stage for the hydrophobic case with Θ=170°.

The already discussed rebounding of the lamella on the hydrophobic surface is clearly visible at the last two instants of dimensionless time in the third column of Figure 4.14. Despite the fact, that we do not observe remarkable differences between the first and second columns associated with the contact angles Θ=10° and Θ=75°, respectively, the vanishing effect of the inertial forces induced by the impact, the different wettabilities will expectedly affect the evolution of the liquid at later stages in these cases as well.

The evolution of the free surface on the hydrophilic solid wall associated with Θ=10° is shown in detail in Figures 4.15 and 4.16 covering also the very later stages. For the low impact velocity case_dry_a, shown in Figure 4.15, a ridge emerges at the outer rim of the liquid lamella as already noted in the discussion above, it is clearly seen here in the contours at the non-dimensional times T=0.78 and T=1.56. It becomes evident again that in the hydrophilic case the wall adhesion force markedly promotes the radial spreading of the wall bounded liquid, so that the ridge on top of the lamella lacks behind. The ridge finally disappears as the spreading proceeds, and the wall becomes continuously wetted by a flat liquid film in the end. The high velocity impact case_dry_b, shown in figure 4.16, exhibits basically the same behaviour, except that the spreading is faster as it is expected.

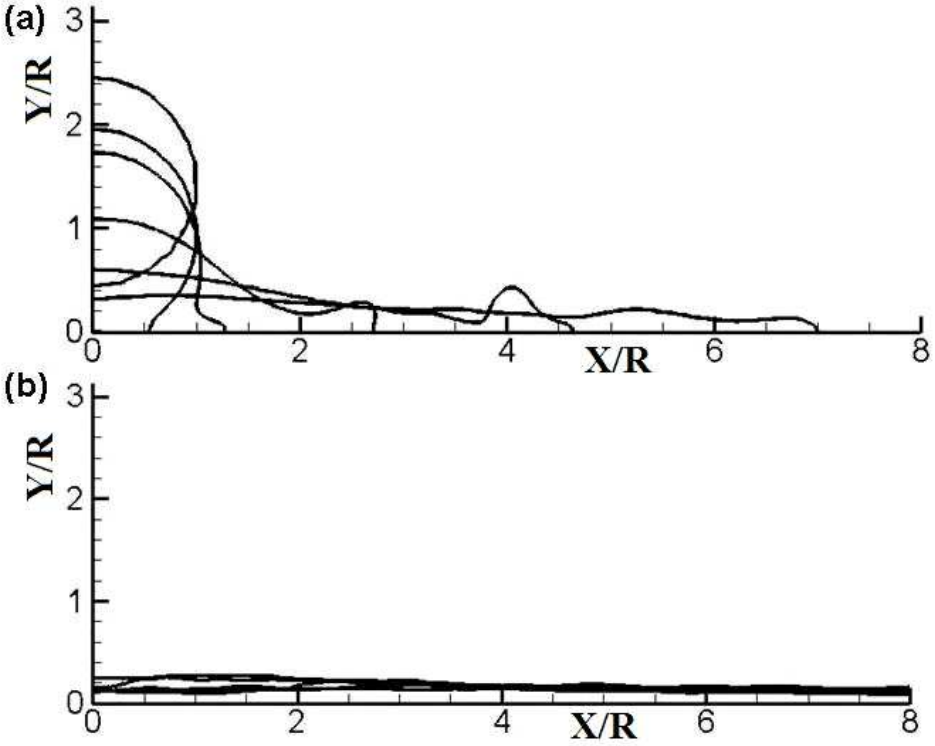

Figure 4.15: Evolution of the free surface for hydrophilic case_dry_a, (a) instantaneous contours at non-dimensional times *T*=0, 0.22, 0.37, 0.78, 1.56 and 2.54, (b) *T*=3.39, 4.40, 5.73, 6.88 and 8.16, respectively

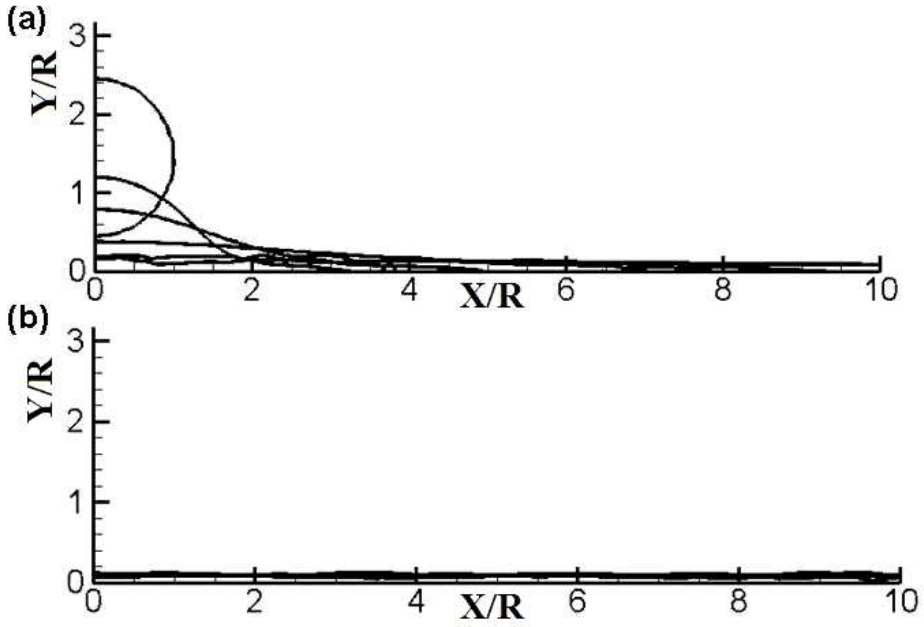

Figure 4.16: Evolution of the free surface for hydrophilic case_dry_b, (a) instantaneous contours at non-dimensional times *T*=0, 0.74, 1.28, 2.77, 5.22 and 8.44, (b) *T*=11.44, 14.06, 19.30, 22.76 and 27.72, respectively

Figure 4.17 gives a more detailed insight into the evolution of the free surface for case_dry_e, associated with a low velocity impact on a hydrophobic surface covering also the later stages. For the first instants of time, the film spreads without the creation of a notable bulge at the outer rim of the liquid sheet. The simulation predicts a wave moving on the top of the film, visible from the shape of the free surface at dimensionless time T=0.78. This particular flow feature was predicted in previous numerical studies as well, but it was not observed by Kannan and Sivakumar (2008) in their experiments in case of hydrophobic surfaces. The wave is moving outwards on top of the liquid sheet with a higher propagation velocity than the wall bounded liquid. It is the origin of the liquid mass which forms a finger-type liquid rim visible at dimensionless time T=1.56. The reason for the slower motion of the wall bounded liquid can be attributed to the non-wettability of the surface. The hydrophobicity basically tends to minimize the contact surface between liquid and solid, which effectively impedes the radial spreading of the contact line. Further on, the liquid finger detaches from the rim and forms the secondary droplet visible in Figure 4.17 (b). The remaining liquid film continues to spread on the surface, and it starts to recede after it has reached its maximum expansion. The tendency to assume the lowest possible surface area is driven by the surface tension. The remaining bulk of the liquid forms a wobbling drop, which finally lifts off from the surface after the receding process. This flow feature is known from an impacting water drop onto a lotus leaf. The prediction of the effect of the detachment of a secondary droplet is difficult to evaluate due to the fact that experimental results are not available, as experimental repeatability for this effect is hardly to achieve.

Figure 4.18 shows the propagation of the free surface for drop impact on the hydrophobic surface with the higher impact velocity. Flow features like the formation of a liquid finger at the rim and the successive generation of the secondary droplets, are observed in an almost similar manner as in the low impact velocity case. The drop spreads however, first to a wider radial expansion resulting in a lower thickness of the liquid film. The reason for the wider spreading is evidently the higher inertia of the impinging drop. The thinner film like the lamely resulting from the wider spread of the liquid get also more easily disrupted, which leads to dry (unwetted) regions and the formation of more secondary drops as seen in Figure 4.18 a.

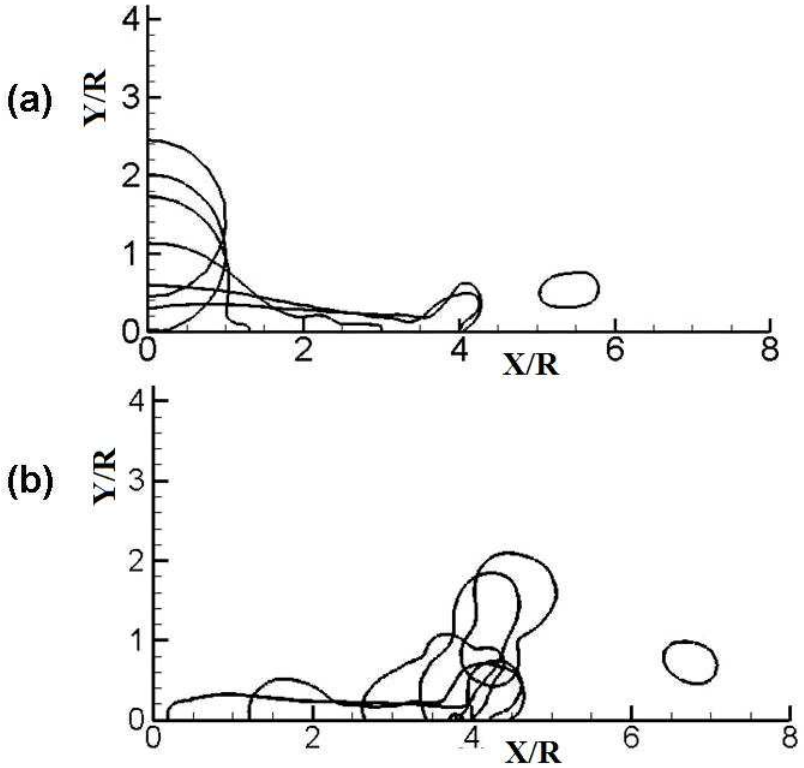

Figure 4.17: Evolution of the free surface for hydrophobic case_dry_e, (a) instantaneous contours at non-dimensional times *T*=0, 0.22, 0.37, 0.78, 1.56 and 2.54, (b) *T*=3.39, 4.40, 5.73, 6.88 and 8.16, respectively

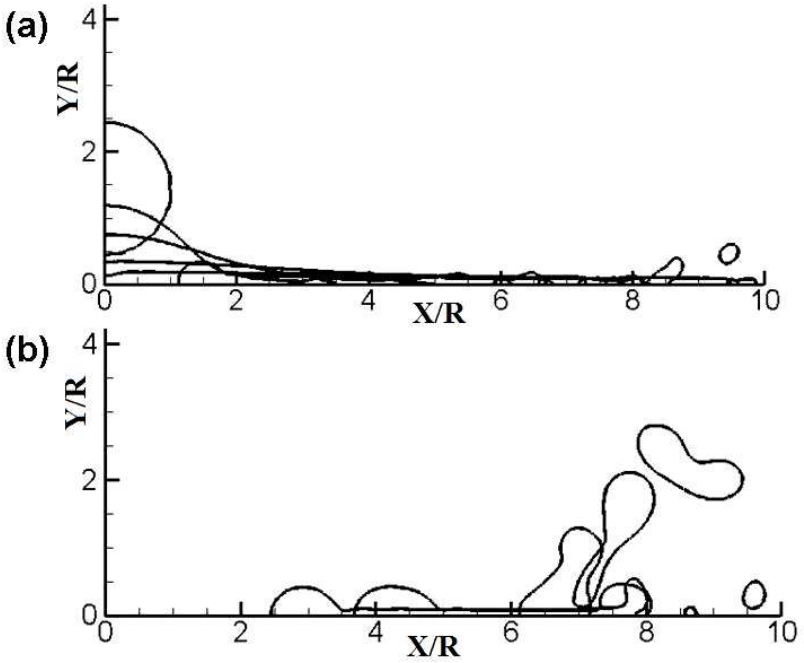

Figure 4.18: Evolution of the free surface for hydrophobic case_dry_f, (a) instantaneous contours at non-dimensional times *T*=0, 0.78, 1.28, 2.77, 5.22 and 8.44, (b) *T*=11.44, 14.06, 19.30, 22.76 and 27.72, respectively

At the later stage, the liquid sheet which remains attached to the wall radially contracts forming bulgy rims at the edges, as shown in Figure 4.18 b. This phenomenon of viscous dewetting followed by a complete lift-off of the remaining liquid from the surface was already observed in the case with the low velocity in Figure 4.17 as well, where it occurred earlier and closer to the centre due to the less intense spreading of the lamella.

In the following, we evaluate our simulation results in a more quantitative way by a comparison against experimental data. Rioboo *et al.* (2002) measured the evolution of the dimensionless spreading diameter in time for various cases of drop impacts on a dry glass surface which represents a highly wettable surface with an advancing contact angle of Θ=10°. The dimensionless spreading diameter $d^* = \frac{2 \cdot r}{D}$ or "spread factor", measuring the radial extension of the liquid relative to the initial drop diameter is plotted over the dimensionless time *T* at the very early stage of the impact process in Figure 4.19. The dotted lines in the figure bound the range of variation of the experimental data obtained for varying initial drop diameters, initial velocities and viscosities. The red line following the power law

$$f = 2.8 \cdot T^{1/2}, \tag{4.4}$$

which represents a best-fit trendline through the experimental data.

Figure 4.19 refers to a hydrophilic liquid-surface combination water on glass, which matches with the wettability conditions of our simulated cases with Θ=10°, considered in case_dry_a and case_dry_b. Our simulation results denoted by the markers in Figure 4.19 agree very well with the trendline obtained from the experiments. The spread factor obtained for the higher impact velocity associated with *We*=537 lies somewhat higher than in the case with the low impact velocity. This tendency is well in line with the experimental findings of Rioboo et al. (2002), who also observed at the early stages a slightly increased spread factor as the impact velocity gets higher. According to their experiments, the differences become notably larger at the later stage beyond $T \approx 0.4$. It should be mentioned, that in reality another physical phenomenon related to the compressibility of the liquid could influence the spreading process at this early stage. Due to the strong compression of the liquid close to the point of the first contact with

the solid wall, a pressure shock wave may be generated and be propagated upwards inside the liquid. This feature is known to appear especially in cases with high impact velocities. Thereby, the pressure shock wave propagating upwards from the stagnation point deforms the shape of the impacting drop before the spreading process actually begins. A deformation of the initial spherical shape of the drop towards a more elliptic shape may therefore influence the spreading due to the change in the curvature of the interface. In addition, the increased static pressure of the liquid compressed by the shock will expectedly lead to a faster initial radial expansion of the liquid near the wall. This very particular phenomenon occurring immediately after the instant of impact can certainly not be reflected by the present simulations due to the assumption of an incompressible liquid flow.

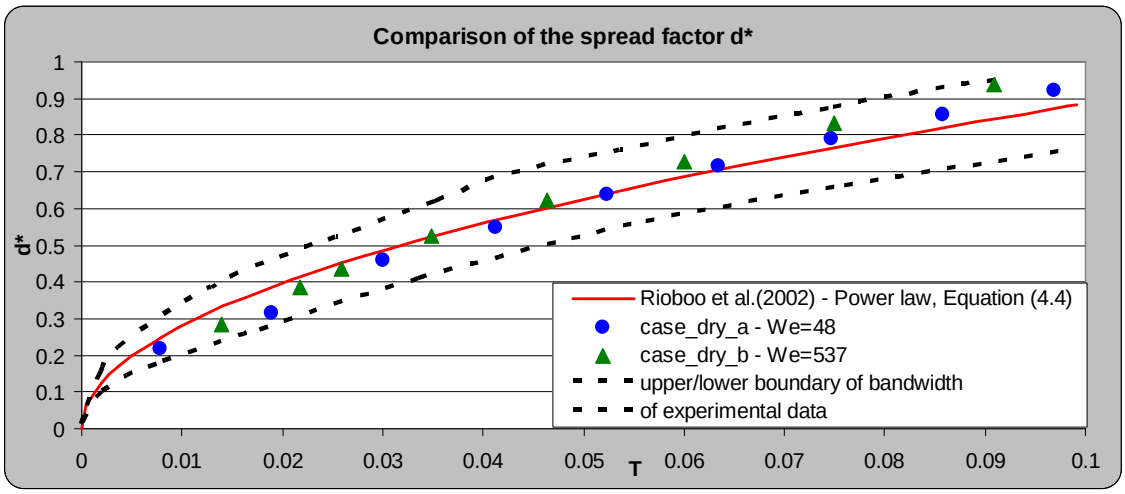

Figure 4.19: Comparison of the spread factor, case_dry_a and case_dry_b, associated with Θ=10°, dashed lines denote the bandwidth of experimental data.

In Figure 4.20 we compare the later stages of the spreading process of case_dry_a, associated with *We*=48 and Θ=10°. The experimental data refer again to the hydrophilic glass surface associated with Θ=10°, measured by Rioboo *et al.* (2002).

The quantitative comparison show quite good agreement with one experimental reference case associated with *We*=35 and *Re*=3102, while for the other two reference cases the agreement is fairly good only until *T*=1. Later, for *T*>1, the disagreement with these data becomes significant. It is remarkable that even the experimental data exhibit much discrepancy at this later stage of spreading, although the Weber and Reynolds numbers do not differ markedly. This points at the experimental difficulties to obtain

reproducible results leading to considerable uncertainties in the data. The observed discrepancy also indicates that the parameterization in terms of two characteristic numbers, *We* and *Re*, may be not sufficient to parameterize the complete spreading/receding process for a given liquid-surface combination.

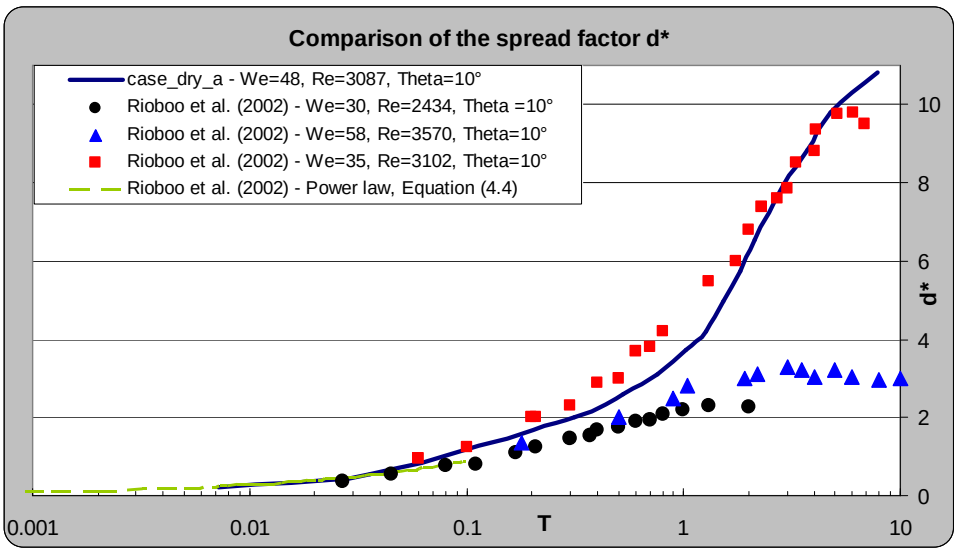

Figure 4.20: Comparison of the spread factor for case_dry_a, at dimensionless time *T*

In Figure 4.21 we compare or simulation results of case_dry_c and case_dry_e against corresponding experimental data of Rioboo *et al.* (2002) to consider the case of medium wettability and hydrophobicity, respectively. The agreement for both cases is fairly good. Case_dry_c shows quite good agreement even for the later stages of the spreading process. The maximum of the simulated spread factor is approximately the same as in the experimental reference case, marked by triangles in Figure 4.21. Case_dry_e shows a notable deviation for the onset of the receding stage, though. The maximum of the simulated spread factor is considerably lower than in the corresponding experiment, marked by bullets in Figure 4.21. Clearly manifested is again the minor influence of the contact angle for the early stages. The influence of the contact angle becomes highly relevant at the later stages of the spreading process. The disagreement between the present simulations and the experiments can be basically attributed to three reasons. First, we observed in our computational results the generation of a secondary droplet emerging from the ridge of the spreading lamella, which can be also seen from the kink in the results for the spread factor occurring at $T>1$ in Figure 4.21. This breakup reduces

the budget of the kinetic energy available for the further radial propagation of the liquid. Secondly, the observed discrepancy for $T>1$ also demonstrates the limits of the wall adhesion model used in the simulations. A simple prescription of a fixed contact angle at the computational cell next to the solid wall does obviously not capture the complex dynamics governing the radial propagation of the contact line. Finally, the surface roughness as one of the most important properties of hydrophobic surfaces is a missing parameter in the present set up. For hydrophobic surfaces, the actually realized water-repellent behaviour depends on the capability to control the morphology of the surface as explained by Minglin and Randal (2006). The microscopic morphology of the surface with length scales of microns and nanometres defines the hydrophobic properties, hence the real value of the contact angle. It is not possible to define such a nanostructure in the present numerical set up. A further critical issue for the simulation is the high demand of spatial resolution near the contact line. Dealing with extremely thin liquid lamellas as in the present case, the resolution is likely to become insufficient to describe accurately the curvature of the liquid-gas interface next to the contact line on the wall.

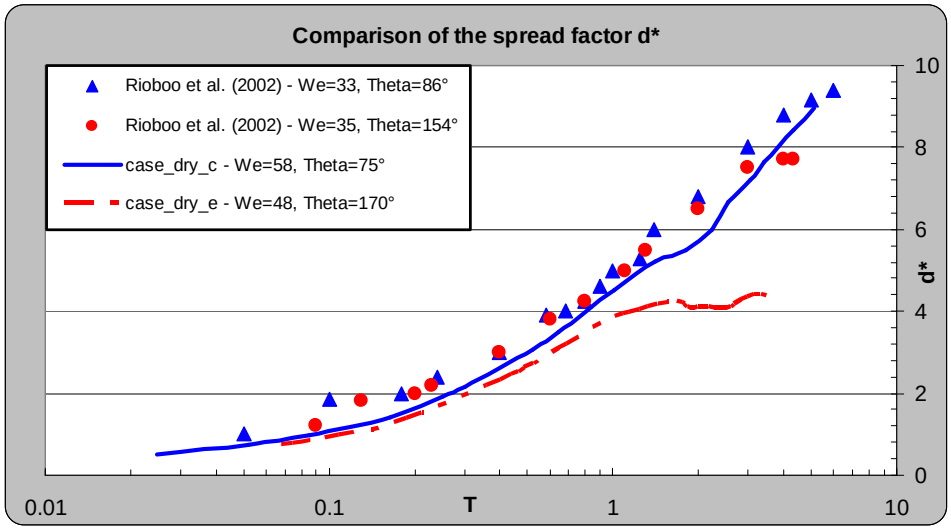

Figure 4.21: Comparison of the spread factor for case_dry_c and case_dry_e

Summing up, it can be noted that the simulations reproduce qualitatively and quantitatively well the flow features which are typically observed after the impact. As such, the simulations are evidently capable to capture the complex flow phenomena during the spreading and eventually rebounding of the liquid which are governed by the complex interaction of the inertial, viscous, wall adhesive, and surface tension forces.

Summary and conclusions

The impact process of a liquid drop on dry and wetted surfaces was simulated using the commercial solver FLUENT 6.3.26. The Volume of Fluid method was used to solve the two-phase flow. A wide range of test cases was simulated with various drop diameters and initial drop velocities. We varied the contact angle at the liquid/solid wall contact line in order to investigate the effect of different wettabilities. The simulation results are compared in qualitative and quantitative manner with experimental observations and data. The work is focussed on the capability of the solver to reproduce realistically the flow behaviour.

The use of a dynamical grid adaptation as presently implemented in the CFD code turned out to be unfeasible. The automatic refinement/coarsening produced unphysical numerical noise in terms of artificial liquid spots and lead also to numerical instabilities. Therefore, a constant mesh was used. An appropriate mesh size was determined based on a comprehensive mesh sensitivity analysis testing different spatial resolutions.

The drop impact on liquid surfaces was simulated with a variation of the initial drop velocity. The qualitative comparison with previous experiments and simulations showed that the present simulations produced realistic results. The increase of the initial drop velocity leads to the ejection of more secondary droplets and to a higher rising of the crown. The occurrence of capillary waves was not observed. A quantitative comparison of the neck velocity at the early stages of the impact against the simulation results of Weiss and Yarin (1999) showed considerable disagreement demonstrating the strong influence of the initial conditions, which were different in these simulations. On the other hand, the radial propagation speed of the crown obtained at the later stage agreed reasonably well with the results of Weiss and Yarin (1999). The present results for the variation of the radial position of the crown with time also followed reasonably well an analytical solution proposed for splash by Yarin and Weiss (1995). This confirms indirectly the assumptions and simplifications which had to be made in the analytical solution.

All in all, it can be stated that the present VoF-based simulations with FLUENT produced reliable results for the impact on wetted surfaces.

The drop impact on dry surfaces was simulated for a wide range of contact angles. A qualitative evaluation of the simulation results showed good agreement with the typically observed behaviour, e.g. the so called Lotus effect in case of a hydrophobic surface. The comparison of the simulated cases themselfes shows the expected effect of a change in the wettability of the solid surface on the flow behaviour. Instead of rebounding and wobbling in case of a hydrophobic surface, the liquid spreads faster and wets a larger area of the surface in case of a more hydrophilic surface. The effect of a higher impact velocity on the spreading process has been investigated as well. Overall, the simulations showed a decreasing influence of the contact angle with an increase of the initial drop velocity. This is well in line with the findings of experimental investigations in the literature.

Quantitative comparisons of the simulated spread rates with experimental data showed generally good agreement with the experimental reference cases. The simulations predicted a realistic spread factor for the early stages of the impact process for all simulated types of surfaces. The very first beginning of the impact process was found to be independent of the contact angle and slightly dependent of the impact velocity. This finding is well in line with experimental observations. The final state of radial expansion of the liquid sheet showed disagreement, especially in case of a hydrophobic surface, where the experiment shows an almost two times wider final radial extension of the liquid. These discrepancies could be explained by several reasons such as the generation of secondary droplets occurring in the simulations, conceptual limits of the applied wall-adhesion model, no account of the microstructure of the surface determining the effective wettability, and eventually insufficient spatial resolution near the contact line.

Except for these inaccuracies affecting the later stage, the simulation of the drop impact onto dry surfaces yielded in general satisfying results. The VoF-based method in combination with the relatively simple wall-adhesion model as implemented in FLUENT was proven as a reliable approach to capture the complex dynamics of the liquid spread on the solid wall seasonably well.

Future Work

The present results always assumed axisymmetric, hence two-dimensional, flow. A next important step would be an extension to a fully three-dimensional simulation to be able to capture realistically specific phenomena triggered by small perturbations into the azimuthal direction like the generation of secondary droplets at the upper rim of the crown in splashes. The strongly increased computational costs of such a three-dimensional simulation will certainly require a robust dynamic refinement of the grid.

A further topic of future investigations would be an improved modelling of the dynamics at the three-phase contact line. As it was revealed by the present simulations, a simple prescription with a constant contact angle in the first computational cell near the wall does not accurately capture the onset of rebounding of the liquid lamella terminating the spreading process.

Literature

Afkhami S., Bussmann M., A. (2006), “Three-Dimensional Model of Droplet Impact Onto an Incline”, *Numerical Simulation of Multiphase Flow with Deformable Interfaces*, Euromech Colloquium 479

Baldacchini T., Carey J.E., Zhou M., Mazur E. (2006), “Superhydrophobic Surfaces Prepared by Microstructuring of Silicon Using a Femtosecond Laser”, *Langmuir*, Volume 22, p.4917-4919

Brackbill J.U., Kothe D. B., Zemach C. (1992), “A Continuum Method for Modeling, Surface Tension”, *Journal for Computional Physics*, 100:335{cited in Fluent 6.3 (2006), p.23-21}

Chandra S., Avedisian C.T. (1991), “On the collision of a droplet with a solid surface”, *Mathematical and Physical Sciences*, Volume 432, p.13-41

Clanet C., Béguin C., Richard D., Quéré D. (2004), “Maximal deformation of an impacting drop”, *Journal of Fluid Mechanics*, Volume 517, p.199-208

Cossali G.E., Coghe A., Marengo M. (1997), “The impact of a single drop on a wetted solid surface”, *Experiments of Fluids*, Volume 22, p. 463-472

Cossali G.E., Coghe A., Marengo M., Zhdanov S. (2004), “The role of time in single drop splash on thin film”, *Experiments in Fluids*, Volume 36, p. 888-900

Davidson M.R. (1999), “Boundary integral prediction of the spreading of an inviscid drop impacting on a solid surface“, *Chemical Engineering Science*, Volume 55, p.1159-1170

De Gennes P.-G., Brockart-Wyart F., Quéré D. (2004), *Capillarity and wetting phenomena*, Springer-Verlag

Fedorchenko A.I., Wang A. (2004), “On some common features of drop impact on liquid surfaces”, *Physics of Fluids*, Volume 16, Number 5, p. 1349-1365

Fedrochenko A.I., Wang A., Wang Y. (2005), “Effect of capillary and viscous forces on spreading of a liquid drop impinging on a solid surface“, *Physics of Fluids*, Volume 17, p.093104

Ferzinger J.H, Peric M. (2002), *Computational Methods for Fluid Dynamics* (3rd ed), Springer-Verlag, Berlin Heidelberg

FLUENT 6.3, *User's Guide*, September 2006, FLUENT Inc. Lebanon NH 03766

Hadfield M. G., Stow C. D. (1981), "An experimental investigation of fluid flow resulting from the impact of a water drop with an unyielding dry surface", *Proceedings of the Royal Society of London. Series A, Mathematical and Physical Sciences*, Vol. 373, p.419-441

Hirt C.R., Nichols B.D. (1981), "Volume of fluid (VOF) method for the dynamics of free boundaries", *Journal of Computational Physics*, Volume 39, p. 201–225

Josserand C., Zaleski S. (2003), "Droplet splashing on a thin liquid film", *Physics of Fluids*, Volume 15, p.1650-1657

Josserand C., Lemoyne L., Troeger R., Zaleski S. (2005), "Droplet impact on a dry surface: triggering the splash with a small obstacle", *Journal of Fluid Mechanics*, Volume 524, p.47-56

Kannan R., Sivakumar D. (2008), "Drop impact process on a hydrophobic grooved surface", *Colloids and Surfaces*, Volume 317, p.697-704

Levin Z., Hobbs P.V. (1971), "Splashing of water drops on solid and wetted surfaces: Hydrodynamics and charge Separation", *Philosophical Transactions of the Royal Society of London. Series A, Mathematical and Physical Sciences*, Vol. 269, No. 1200 (May 13, 1971), p. 555-585

López J., Hernández J., Gómez P. (2008), "A new volume of fluid method in three dimensions – Part I: Multidimensional advection method with face-matched flux polyhedra", *International Journal for Numerical Methods in Fluids*, Number 58, p.897-921

Ma M., Hill R.M. (2006), "Superhydrophobic Surfaces", *Current Opinion in Colloid and Interface Science*, Volume 11, p.193-202

Morton D., Rudman M., Jong-Leng L. (2000), "An investigation of the flow regimes resulting from splashing drops", *Physics of Fluids*, Volume 12, p.747-763

Mukherjee S., Abraham J. (2007), “Investigation of drop impact on dry walls with a lattice-Bolzmann model“, *Journal of Colloid and Interface Science*, Volume 312, p.341-354

Mundo Chr., Sommerfeld M, Tropea C. (1995), “Droplet-wall collisions: experimental studies of the deformation and break-up process”, *International Journal for Multiphase Flow*, Volume 21, p. 151-173

Nikolopoulos N., Theodorakakos A., Bergeles G. (2005), “Normal impingement of a droplet onto a wall film: a numerical investigation“, *International Journal of Heat and Fluid Flow*, Volume 26, p.:119-132

Popinet S., Zaleski S. (1999), “A Front-Tracking Algorithm for accurate Representation of Surface Tension“, *International Journal for Numerical Methods in Fluids*, Number 30, p.775-793

Quéré D. (2002), “Fakir Droplets”, *Nature Materials,*Volume 1, p.14-15

Rein M. (1993), “Phenomena of liquid drop impact on solid and liquid surfaces“, *Fluid Dynamics Research*, Volume 12, p.61-93

Rein M. (2002), “Capillary effects at newly formed liquid-liquid contacts“, *Physics of Fluids*, Volume 14, Number 1, p.411-414

Rieber M., Frohn A. (1999), “A numerical Study on the Mechanism of Splashing“, *International Journal of Heat and Fluid Flow*, Volume 20, p.455-461

Rioboo R., Tropea C., Marengo M. (2001), “Outcomes from a Drop Impact on solid Surfaces“, *Atomization and Sprays*, Volume 11, p. 155-165

Rioboo R., Marengo M., Tropea C. (2002), “Time evolution of liquid drop impact onto solid, dry surfaces“, *Experiments in Fluids*, Volume 33, p.112-124

Rioboo R., Bauthier C., Conti J., Voue M. Conick J.D. (2003), “Experimental investigation of splash and crown formation during single drop impact on wetted surfaces“, *Experiments in Fluids*, Volume 35, p 648-652

Roisman I.V., Tropea C. (2002), “Impact of a drop onto a wetted wall: description of crown formation and propagation“, *Journal of Fluid Mechanics*, Volume 472, p.373-397

Schroll R. D., Josserand C., Zaleski S., Zhang W. W. (2009), “Impact of a viscous liquid drop“, University of Chicago, Physics Department and the James Franck Institute

Shi Z., Yan Y., Yang F., Quian Y., Hu G. (2008), “A lattice Boltzmann method for simulation of a three-dimensional drop impact on a liquid film“, *Journal of Hydrodynamics*, Volume 20, p.267-272

Vander Wal R.L., Berger G.M., Mozes S.D. (2006), “The splash/non-splash boundary upon a dry surface and thin fluid film“, *Experiments in Fluids*, Volume 40, p.53-59

Weiss D.A., Yarin A.L. (1999), “Single drop impact onto liquid films neck distortion, jetting, tiny bubble entrainment and crown formation“, *Journal of Fluid Mechanics*, Volume 385, p.229-254

Xie H., Koshizuka S., Oka Y. (2004), “Numerical simulation of liquid drop deposition in annular-mist flow regime of boiling water reactor”, *Journal of Nuclear Science and Technique*, Volume 41, p. 569-578

Xu L., Wendy W., Zhang W. (2005), “Drop splashing on a dry smooth surface”, *Physical Review* Letters, Volume 94, Issue 18

Yarin A.L., Weiss D.A. (1995), “Impact of drops on solid surfaces: self-similar capillary waves, and splashing as a new type of kinematic discontinuity”, *Journal of Fluid Mechanics*, Volume 283, p. 141-173

Yarin A.L. (2006), “Drop impact dynamics: splashing, spreading, receding, bouncing”, *Annual Review of Fluid Mechanics*, Volume 38, p. 159-192

Appendices

Appendix A:

User Defined Function

User Defined Function's (UDF) are programmed functions to enhance the baseline capability of FLUENT. Conditions of the flow field and special features of the flow, e.g. boundary conditions, material properties or functions for the mass transfer can be specified and incorporated via input files. They are written in the C programming language, and can contain several UDF's and macros.

For the considered cases UDFs were used to initialize the flow field with the allocation of the phases and to initialize the drop velocity. The name of the used macro is DEFINE_INIT, and it produces the same result as the initialization with patching in the FLUENT Graphical User Interface (GUI) does. Once the source file is added and the functions are linked to the solver it is executed only once at the initialization. A pointer is used to provide access to the cell threads in the mesh. Each property needs its own macro. Therefore three macros were programmed. The first one serves for the allocation of the primary phase, which is defined as the liquid phase, hence it allocates the drop and the liquid wall film. The second macro allocates the secondary phase air to the rest of the domain. The last macro allocates the drop velocity to the corresponding cells. An example for the impact of a drop onto a liquid film is given below.

Appendix B:

The following UDF code initialize the flow domain as is was used for case_b, the impact of a liquid drop onto a thin liquid film.

```
/*************************************************************************
udf_gattringer - case_b
UDF for specifying initial conditions
 distinguish phases -executed once at the beginning of the solution process--*/
/*************************************************************************/
#include "stdio.h"
#include "udf.h" /* must be at the beginning of every UDF */
#include "math.h"
#define radius 0.0017
```

```
#define phi_start -3.1415
#define phi_end 3.1415
#define h_film 0.00043
#define h_drop 0.00218
#define velocity -1.3
/*drop velocity*/
/* domain pointer that is passed by INIT function is mixture domain */
DEFINE_INIT(init_drop_velocity, mixture_domain)
{   int phase_domain_index;       /* index of subdomain pointers 0 for the primary phase, and is incremented
                                                                        by one for each secondary phase in the mixture*/
  cell_t cell;
  Thread *cell_thread;
  Domain *subdomain;                                  /*pointer to the phase-level domain*/
  real xc[ND_ND];
              /* loop over all subdomains (phases) in the superdomain (mixture) */
          sub_domain_loop(subdomain, mixture_domain, phase_domain_index)
  {                   /* loop if secondary phase */
                      if (DOMAIN_ID(subdomain) == 2)
                      /* loop over all cell threads in the secondary phase domain */
                      thread_loop_c (cell_thread,subdomain)
                      {                                   /* loop over all cells in secondary phase cell threads */
                                  begin_c_loop_all (cell,cell_thread)
                                      {           C_CENTROID(xc,cell,cell_thread);
                                                  if (sqrt(pow(xc[0] - 0.0, 2.)+pow(xc[1] - h_drop, 2.)) <= radius)
                                                       /*set drop velocity to 1 for centroid */
                                                      C_V(cell,cell_thread) = velocity;
                                      }
                                      end_c_loop_all (cell,cell_thread)
                              }
          }
}
/*-------------------------------------------------------------------------------*/
 /*drop liquid*/
/* domain pointer that is passed by INIT function is mixture domain */
DEFINE_INIT(init_liquid_phase, mixture_domain)
{   int phase_domain_index;       /* index of subdomain pointers 0 for the primary phase, and is incremented
                                                                        by one for each secondary phase in the mixture*/
  cell_t cell;
  Thread *cell_thread;
  Domain *subdomain;                                  /*pointer to the phase-level domain*/
  real xc[ND_ND];
   /* loop over all subdomains (phases) in the superdomain (mixture) */
          sub_domain_loop(subdomain, mixture_domain, phase_domain_index)
  {                   /* loop if secondary phase */
```

```
                if (DOMAIN_ID(subdomain) == 2)
                /* loop over all cell threads in the secondary phase domain */
                thread_loop_c(cell_thread,subdomain)
                        {       /* loop over all cells in secondary phase cell threads */
                                begin_c_loop_all (cell,cell_thread)
                                        {       C_CENTROID(xc,cell,cell_thread);
                                if ((sqrt(pow(xc[0] - 0.0,2.)+pow(xc[1] - h_drop,2.)) <= radius) || ((xc[1]) <= h_film))
                                         /*set volume fraction to 1 for centroid for phase 2*/
                                        C_VOF(cell,cell_thread) = 1.;
                                        else
                                /* otherwise initialize to zero ! for C_VOF the else is necessary*/
                                                C_VOF(cell,cell_thread) = 0.;
                                }
                                end_c_loop_all (cell,cell_thread)
                        }
        }
}
/*---------------------------------------------------------------------------*/
 /*air liquid*/
/* domain pointer that is passed by INIT function is mixture domain */
DEFINE_INIT(init_air_phase, mixture_domain)
{   int phase_domain_index;     /* index of subdomain pointers 0 for the primary phase, and is incremented
                                        by one for each secondary phase in the mixture*/
  cell_t cell;
  Thread *cell_thread;
  Domain *subdomain;                    /*pointer to the phase-level domain*/
  real xc[ND_ND];
   /* loop over all subdomains (phases) in the superdomain (mixture) */
        sub_domain_loop(subdomain, mixture_domain, phase_domain_index)
  {
                /* loop if secondary phase */
                if (DOMAIN_ID(subdomain) == 3)
                /* loop over all cell threads in the secondary phase domain */
                thread_loop_c(cell_thread,subdomain)
                        {       /* loop over all cells in secondary phase cell threads */
                                begin_c_loop_all (cell,cell_thread)
                                        {       C_CENTROID(xc,cell,cell_thread);
                                if ((sqrt(pow(xc[0] - 0.0,2.)+pow(xc[1] - h_drop,2.)) > radius) && ((xc[1]) > h_film))
                                         /*set volume fraction to 1 for centroid for phase 3*/
                                                C_VOF(cell,cell_thread) = 1.;
                                        else
                                /* otherwise initialize to zero ! for C_VOF the else is necessary */
                                                C_VOF(cell,cell_thread) = 0.;
                                }
```

```
                end_c_loop_all (cell,cell_thread)
            }
        }
}
```

Appendix C:

Grids used for the grid sensitivity study with the respective adjustment in the meshing tool GAMBIT.

Grid	Number of Cells	Interval Size (GAMBIT)
Mesh 1	87 100	0.1
Mesh 2	137 700	0.08
Mesh 3	177 900	0.07
Mesh 4	206 300	0.065

Table A.1: Meshes used for the grid sensitivity study

Appendix D:

A short overview over the case parameters and FLUENT settings.

The tables give the important flow and FLUENT setting parameter. The Courant number can be specified in the multiphase panel while the global courant numbers are set in the start iteration panel. In the Under-Relaxation Factors (URF) column, the sequences of values refer to the solution of the following quantities: Pressure/Density/Body Forces/Momentum/Energy.

The values in brackets are the starting values for the pressure-velocity scheme, or the corresponding input properties. Generally the first order spatial discretization has been used for the first time steps only. It was switched to second order scheme after a stable run was ensured.

Case	Impact Velocity	*We* number	*Re* number	Courant number	URF	Global Courant
case_a (SIMPLE)	0.1 m/s u_{WY}=0.77	1.2	224	0.1	0.3/0.6/0.6/0.7/0.6 (0.1/1/1/0.7/1)	1 (0.1)
case_b (PISO)	1.3 m/s u_{WY}=10	203	2910	0.1	0.2/0.2/0.2/0.2/0.9 (0.1/1/1/0.7/1)	0.9 (0.1)
case_c (PISO)	2.6 m/s u_{WY}=20.1	811	5820	0.1	0.1/1/1/0.7/1	0.8 (0.1)

Table A.2: Case data for drop impact on liquid surface

Case	Impact velocity	*We* number	*Re* number	Courant number	URF	Global Courant
Case_dry_a	1.12	48	3087	0.1	0.1/1/1/0.7/1 (0.1/1/1/0.7/1)	0.9 (0.1)
Case_dry_b	3.76	537	10365	0.1	0.1/1/1/0.7/1 (0.1/1/1/0.7/1)	0.8 (0.2)

Table A.3: Case data for drop impact on dry surfaces – variation of the impact velocity

Case	Contact angle θ	D (*We*)	*Re* number	Courant number	URF	Global Courant
case_dry_c (PISO)	170°	3.04mm (58)	3570	0.1 (0.05)	0.1/1/1/0.7/0.2 (0.1/1/1/0.7/0.2)	2 (0.1)
case_dry_d (PISO)	75°	2.75mm (52)	3230	0.1 (0.05)	0.1/1/1/0.7/0.2 (0.1/1/1/0.7/0.2)	2 (0.1)

Table A.4: Case data for drop impact on dry surfaces – variation of the contact angle

Case	Impact velocity	*We* number	*Re* number	Courant number	URF	Global Courant
Case_dry_e	1.12	48	3087	0.1	0.1/1/1/0.7/1 (0.1/1/1/0.7/1)	0.9 (0.1)
Case_dry_f	3.76	537	10365	0.1	0.1/1/1/0.7/1 (0.1/1/1/0.7/1)	0.8 (0.2)

Table A.5: Case data for drop impact on hydrophobic surface – variation of the velocity